



# Cosmological Vlasov–Poisson Simulations of Structure Formation with Relic Neutrinos: Nonlinear Clustering and the Neutrino Mass

Kohji Yoshikawa<sup>1</sup> , Satoshi Tanaka<sup>2</sup> , Naoki Yoshida<sup>3,4,5</sup> , and Shun Saito<sup>4,6</sup>

<sup>1</sup> Center for Computational Sciences, University of Tsukuba, 1-1-1 Tennodai, Tsukuba, Ibaraki 305-8577, Japan; [kohji@ccs.tsukuba.ac.jp](mailto:kohji@ccs.tsukuba.ac.jp)

<sup>2</sup> Yukawa Institute for Theoretical Physics, Kyoto University, Kitashirakawa Oiwake-Cho, Sakyo-Ku, Kyoto 606-8502, Japan

<sup>3</sup> Department of Physics, The University of Tokyo, Bunkyo, Tokyo 113-0033, Japan

<sup>4</sup> Kavli Institute for the Physics and Mathematics of the Universe, The University of Tokyo, Kashiwa, Chiba 277-8583, Japan

<sup>5</sup> Research Center for the Early Universe, The University of Tokyo, Bunkyo, Tokyo 113-0033, Japan

<sup>6</sup> Institute for Multi-messenger Astrophysics and Cosmology, Department of Physics, Missouri University of Science and Technology, 1315 N Pine St, Rolla, MO 65409, USA

Received 2020 August 2; revised 2020 September 28; accepted 2020 September 28; published 2020 November 30

## Abstract

We present the results of cosmological simulations of large-scale structure formation with massive neutrinos. The phase-space distribution of the cosmic relic neutrinos is followed, for the first time, by directly integrating the six-dimensional Vlasov–Poisson equations. Our novel approach allows us to represent free streaming and clustering of neutrinos, and their gravitational interaction with cold dark matter accurately. We thus obtain solutions for the collisionless dynamics independent of conventional  $N$ -body methods. We perform a suite of hybrid  $N$ -body/Vlasov simulations with varying the neutrino mass, and systematically examine the dynamical effects of massive neutrinos on large-scale structure formation. Our simulations show characteristic large-scale clustering of the neutrinos and their coherent streaming motions relative to dark matter. The effective local neutrino “temperature” around massive galaxy clusters varies by several percent with respect to the cosmic mean; the neutrinos in clusters can be hotter or colder depending on the neutrino mass. We study a number of statistics of the large-scale structure and of dark matter halos in comparison with those obtained by  $N$ -body simulations and/or by perturbation theory. Our simulations mark an important milestone in numerical cosmology, and pave a new way to study cosmic structure formation with massive neutrinos.

*Unified Astronomy Thesaurus concepts:* [Cosmological neutrinos \(338\)](#); [Neutrino masses \(1102\)](#); [Cosmological parameters from large-scale structure \(340\)](#); [Large-scale structure of the universe \(902\)](#)

## 1. Introduction

A generic prediction of the standard Big Bang cosmology is the existence of a relic neutrino background that pervades the universe. Neutrinos had been long considered to be massless in the standard model of particle physics, but the experimental confirmation of neutrino flavor oscillation (Fukuda et al. 1998) suggests that at least two of the three kinds of neutrinos have nonzero masses. However, their absolute masses and the hierarchy among the three mass eigenstates remain unknown, and precise measurement of the neutrino mass by terrestrial experiments is still challenging.

The dynamical influence of the permeating relic neutrinos is imprinted in the large-scale mass distribution in the universe. The major effect of massive neutrinos is suppression of clustering of dark matter and hence of galaxies. Collisionless damping caused by fast-moving neutrinos effectively “drags” the growth of structure, which can be discerned, for instance, as suppression of the galaxy power spectrum at smaller scale than the neutrinos free-streaming scale. The free-streaming scale and the degree of damping depend on the absolute mass of neutrinos (see Lesgourgues & Pastor 2006 for a detailed review). Thus, it is possible to constrain or even *measure* the absolute mass of neutrinos and their mass hierarchy from observations of the large-scale structure (LSS) in the universe (e.g., Hu et al. 1998; Takada et al. 2006; Saito et al. 2009; Namikawa et al. 2010; Font-Ribera et al. 2014; Boyle & Komatsu 2018; Chudaykin & Ivanov 2019).

The most stringent constraints on the absolute mass of neutrinos are given by observations of the CMB anisotropies

(Planck Collaboration et al. 2020). The total mass of three mass eigenstates of neutrinos is estimated to be smaller than 0.26 eV (95% C.L.) with the Planck data alone, and a tighter constraint of 0.12 eV is derived from the combination with the CMB lensing as well as with the baryon acoustic oscillation (BAO) data.

It is of crucial importance to provide an accurate theoretical prediction of the dynamical effect of the relic neutrinos particularly in nonlinear regime, in order to place tight constraint on the absolute neutrino masses. To this end, a number of authors use perturbation theory and/or attempt analytical modeling of the evolution of density fluctuations under the presence of massive neutrinos (e.g., Saito et al. 2008; Wong 2008; Lesgourgues et al. 2009; Shoji & Komatsu 2009; Blas et al. 2014; Dupuy & Bernardeau 2015; Führer & Wong 2015; Peloso et al. 2015; Levi & Vlah 2016; Senatore & Zaldarriaga 2017). Ichiki & Takada (2012) investigate the dynamical effect of massive neutrinos on nonlinear spherical collapse of cold dark matter (CDM) halos starting from a top-hat CDM overdensity. They show that massive neutrinos effectively suppress the mass function of dark matter (DM) halos even if the total neutrino mass is lightest possible inferred from the neutrino oscillation experiments, 0.05 eV or 0.1 eV for the normal and inverted mass hierarchy, respectively. Despite the theoretical challenges, the LSS observables are shown to derive competitive constraints on the total neutrino masses (e.g., Seljak et al. 2006; Ichiki et al. 2009; Thomas et al. 2010; Saito et al. 2011; Zhao et al. 2013; Beutler et al. 2014; Alam et al. 2017; Aviles & Banerjee 2020; Ivanov et al. 2020; Palanque-Delabrouille et al. 2020).

Direct numerical simulations have been used to study the dynamical impact of massive neutrinos on the LSS formation (e.g., Brandbyge & Hannestad 2009, 2010; Brandbyge et al. 2010; Viel et al. 2010; Bird et al. 2012; Ali-Haïmoud & Bird 2013; Castorina et al. 2014; Upadhye et al. 2014; Villaescusa-Navarro et al. 2014, 2020; Inman et al. 2015, 2017; Banerjee & Dalal 2016; Wright et al. 2017; Banerjee et al. 2018; McCarthy et al. 2018). Many of these simulations employ particle-based techniques and attempt to reproduce free-streaming of massive neutrinos by adding thermal velocities randomly sampled according to the velocity distribution function of massive neutrinos. The validity of such treatment is unclear, however. Also the particle-based simulation method generically suffers from numerical shot noise owing to relatively coarse sampling of neutrino distribution in the six-dimensional phase-space (Yoshikawa et al. 2013). Poor sampling in the velocity space leads to inaccurate treatment of the free-streaming, because the high velocity tails of the distribution function, a dynamically crucial component, is not smoothly represented.

As a possible remedy to reduce the particle shot noise, grid-based approaches (Brandbyge & Hannestad 2009; Viel et al. 2010) and a hybrid method with a particle-based one (Brandbyge & Hannestad 2010) are proposed. In the latter, the density field of massive neutrinos is *assumed* to evolve according to linear theory. Unfortunately, these approximate methods do not follow nonlinear evolution of neutrino dynamics and the gravitational interaction with the CDM component consistently. Recently, Inman et al. (2015, 2017) performed  $N$ -body simulations employing an extremely large number of particles to reduce the shot-noise contamination. While employing a large number of particles is a straightforward way to mitigate discreteness effects, it would be desirable to devise and use a method that can accurately represents the velocity distribution function and follow its time evolution.

In this paper, we present a novel approach that directly follows the time evolution of the distribution function of neutrinos in six-dimensional phase-space. We directly solve the collisionless Boltzmann equation, or the Vlasov equation, using a finite-volume method. Since our approach treats massive neutrinos as a continuous collisionless *fluid*, it is not compromised by numerical shot noise. This approach, which is referred to as Vlasov simulation hereafter, was first applied to numerical simulations of self-gravitating systems by Fujiwara (1981, 1983a), and also applied to DM halo formation with massive neutrinos (Fujiwara 1983b), although limited in one or two spatial dimensions. A number of Vlasov solvers have been developed with employing various methods and have been applied to plasma and self-gravitating systems (Filbet & Sonnendrücker 2003; Colombi & Touma 2014; Colombi & Alard 2017). The simulations of Yoshikawa et al. (2013) are the first of the kind that are performed with three spatial dimensions (in six-dimensional phase-space). The Vlasov simulations are able to accurately reproduce free-streaming of a collisionless fluid, an effect expected to be of critical importance in following the dynamics of cosmological relic neutrinos. In the present paper, we run a series of Vlasov simulations of the LSS formation with massive neutrinos, and study the clustering and the dynamical effect of neutrinos systematically with varying the total neutrino mass.

The rest of the paper is organized as follows. We describe our new numerical method presented in this work in Section 2.

Sections 3 and 4 are devoted to describe numerical simulations and their results regarding the dynamical effect of massive neutrinos on the LSS formation. In Section 5, we address the computational cost of our Vlasov simulation and the conventional  $N$ -body simulations in terms of the amount of memory Requirement, computational wall clock time, and the spatial resolution of neutrinos' distribution. Finally, we summarize our work in Section 6.

## 2. Formulation and Numerical Method

We adopt a novel numerical scheme that follows the distribution of the neutrinos by directly integrating the Vlasov equation in the full six-dimensional phase-space. For the CDM component, we perform high-resolution  $N$ -body simulations because CDM is assumed to have a very small thermal velocity dispersion with a very compact distribution in velocity space. The efficient hybrid  $N$ -body/Vlasov simulations allow us to reproduce the nonlinear clustering of CDM and neutrinos in a self-consistent manner. In this section, we lay out basic theoretical formulation for the dynamics of CDM and neutrinos in a cosmological context.

### 2.1. Cosmological Relic Neutrinos

In the hot primeval plasma in the early universe, neutrinos are in thermal equilibrium with radiation and with other matter, and have a Fermi–Dirac distribution. After the neutrinos decouple from other matter, the distribution function freezes out because the neutrinos have little interaction with other component afterwards. Neutrinos with nonzero masses become nonrelativistic at some early epoch, and then the velocity distribution function is given by

$$F_{\text{FD}}(\mathbf{v}, t) = \left[ \exp\left(\frac{m_\nu |\mathbf{v}|}{k_B T_\nu}\right) + 1 \right]^{-1}, \quad (1)$$

where  $m_\nu$  is a mass eigenvalue of neutrinos,  $c$  the speed of light,  $k_B$  the Boltzmann constant,  $T_\nu$  the redshifted mean “temperature,” and  $\mathbf{v}$  is the peculiar velocity of neutrinos. Here, we do not consider the chemical potential of neutrinos because it is thought to be negligible. The temperature of the cosmic neutrino background is proportional to, and slightly lower than, that of the cosmic microwave background (CMB) photons  $T_{\text{CMB}}$  as

$$T_\nu = \left(\frac{4}{11}\right)^{1/3} T_{\text{CMB}}. \quad (2)$$

The numerical factor originates from photon heating during a brief period of electron–positron annihilation. The comoving number density of neutrinos,  $n_\nu$ , can be obtained by integrating (1) over the entire velocity space, and the density parameter of nonrelativistic neutrinos at the present universe is given by

$$\Omega_\nu = \sum_i n_\nu m_\nu^i c^2 / \rho_c = \frac{M_\nu c^2}{93.14 h^2 \text{eV}}, \quad (3)$$

where  $\rho_c$  is the critical energy density,  $h$  is the present value of the Hubble parameter in units of  $100 \text{ km s}^{-1} \text{ Mpc}^{-1}$ ,  $m_\nu^i$  is the neutrino mass of the  $i$ th mass eigenstate, and  $M_\nu$  is the sum of three mass eigenvalues of neutrinos.

## 2.2. Vlasov Simulation of Neutrinos

The Vlasov equation describing the dynamics of neutrinos in the cosmological comoving frame is given by

$$\frac{\partial f}{\partial t} + \frac{\mathbf{u}}{a^2} \cdot \frac{\partial f}{\partial \mathbf{x}} - \frac{\partial \phi}{\partial \mathbf{x}} \cdot \frac{\partial f}{\partial \mathbf{u}} = 0 \quad (4)$$

where  $f(\mathbf{x}, \mathbf{u}, t)$  is the distribution function of neutrinos,  $\phi(\mathbf{x})$  is the gravitational potential,  $a(t)$  is the scale factor of cosmological expansion,  $\mathbf{x}$  is the comoving coordinate, and  $\mathbf{u} = a^2 \dot{\mathbf{x}}$  is the canonical velocity. The canonical velocity is convenient as a “velocity” variable in our Vlasov simulations because the neutrino peculiar velocity  $a\dot{\mathbf{x}}$  decay as  $a(t)^{-1}$  in the limit of the uniform and homogeneous universe. Then the canonical velocity remains roughly constant in the linear evolution phase. Note also that the bulk velocity of the neutrinos is typically much smaller than, or only comparable to, the velocity dispersion. These features are numerically convenient because the extent of the velocity distribution in the initial condition does not vary significantly in terms of canonical velocity. We refer the readers to the [Appendix](#) for more detailed discussion on the choice of velocity coordinate such as peculiar velocity.

The distribution function is normalized so that the integration over the velocity space yields the mass density *contrast* as

$$\int f(\mathbf{x}, \mathbf{u}, t) d^3\mathbf{u} = 1 + \delta_\nu(\mathbf{x}, t), \quad (5)$$

where  $\delta_\nu(\mathbf{x}, t)$  is the mass density fluctuation of the neutrinos.

As in Yoshikawa et al. (2013), the six-dimensional phase-space is discretized onto uniform cartesian mesh grids (hereafter Vlasov mesh grids) both in the physical and velocity spaces in a finite-volume manner. The number of mesh grids is referred to as  $N_x$  for the physical space, and  $N_u$  for the velocity space, respectively. We configure cubic physical and velocity domains with  $0 \leq x, y, z \leq L_{\text{box}}$  and  $-u_{\text{max}} \leq u_x, u_y, u_z \leq u_{\text{max}}$ .

We adopt the directional splitting method to solve Equation (4). We effectively solve six one-dimensional advection equations as

$$\frac{\partial f}{\partial t} + \frac{u_i}{a^2} \frac{\partial f}{\partial x_i} = 0 \quad (i = 1, 2, 3) \quad (6)$$

and

$$\frac{\partial f}{\partial t} - \frac{\partial \phi}{\partial x_i} \frac{\partial f}{\partial u_i} = 0 \quad (i = 1, 2, 3), \quad (7)$$

where  $(x_1, x_2, x_3) = (x, y, z)$  and  $(u_1, u_2, u_3) = (u_x, u_y, u_z)$ . These advection equations are numerically solved with the SL-MPP7 scheme (Tanaka et al. 2017), which has spatially seventh-order accuracy and ensures the monotonicity and positivity of the numerical solution.

We adopt outflow boundary conditions in the velocity space. If a fraction of neutrinos are accelerated beyond the predefined velocity boundaries, they are simply treated as disappeared. Our simulation code automatically detects such an unphysical situation and monitors the conservation of total mass of neutrinos. In practice, we configure a large enough velocity space and the total loss from the velocity boundaries is sufficiently small and the fractional error of mass conservation is less than 0.001%. We impose periodic boundary conditions

on the physical space as is often adopted in cosmological simulations.

## 2.3. N-body Simulation of CDM

We employ the conventional  $N$ -body method for CDM. We assume that the simulation particles represent baryons and CDM, and do not treat them separately nor consider the hydrodynamic effect of baryons. Hereafter, the combined component of CDM and baryons is referred to as “CDM” for simplicity.

The motion of each particle is determined by the equation of motion

$$\frac{d^2\mathbf{x}}{dt^2} + 2H\frac{d\mathbf{x}}{dt} = -\frac{\nabla\phi}{a^2}, \quad (8)$$

where  $H(t) \equiv \dot{a}/a$  is the Hubble parameter. We adopt a leapfrog integrator as described in Section 2.5. We compute the gravitational forces on  $N$ -body particles with particle-mesh (PM) scheme (Hockney & Eastwood 1981). The Poisson solver is modified suitably to incorporate the gravitational interaction of neutrinos with CDM.

## 2.4. Gravitational Potential

The gravitational potential in Equation (8) is the same as in Equation (4). Thus both CDM and neutrinos share the common gravitational field, which satisfies the Poisson equation

$$\nabla^2\phi = 4\pi G\bar{\rho}_m(t)a^2\delta_m, \quad (9)$$

where  $\bar{\rho}_m(t)$  and  $\delta_m$  are the mean mass density and its fluctuation of the total matter composed of CDM and neutrinos.

For a given distribution of CDM particles, we compute the density field using the Triangular Shaped Cloud (TSC) scheme on a uniform mesh grid (hereafter the PM mesh) with  $N_{\text{PM}}$  grid points. The density field of neutrinos is computed at  $N_x$  spatial grid points employed in the Vlasov simulation. We integrate (sum) the discretized distribution function over the velocity space. Since  $N_{\text{PM}}$  is set to be larger than  $N_x$ , the total matter (CDM + neutrinos) density is obtained by up-sampling the neutrino density field by  $N_{\text{PM}}/N_x$ -fold and then by adding the contribution to the CDM density. The Poisson Equation (9) is numerically solved with the convolution method (Hockney & Eastwood 1981) that applies fast Fourier transform to the total matter density field. The gradient of the gravitational potential is evaluated by the four-point finite difference approximation (FDA), and is interpolated at positions of  $N$ -body particles with the TSC scheme. When integrating the Vlasov equation, the gravitational potential on the PM mesh is down-sampled onto the Vlasov mesh, and the gravitational force in Equation (4) is computed with the six-point FDA scheme.

## 2.5. Time Integration

The time step width for integrating Equations (4) and (8) is constrained by the conditions in the  $N$ -body simulation for CDM and in the Vlasov simulation for neutrinos. In the  $N$ -body simulation, the time step  $\Delta t_N$  is determined as

$$\Delta t_N = \min \left( \min_i \left( \frac{\Delta_{\text{PM}}}{|\dot{\mathbf{x}}_i|} \right), \min_i \left( \sqrt{\frac{\Delta_{\text{PM}}}{|\nabla\phi_i|/a^2}} \right) \right), \quad (10)$$

where  $\nabla\phi_i$  is the gradient of gravitational potential at the position of  $i$ th  $N$ -body particle,  $\Delta_{\text{PM}} = L_{\text{box}}/N_{\text{PM}}^{1/3}$  the grid spacing of the PM mesh. We search the global minimum by considering the above two criteria for all the  $N$ -body particles.

In the Vlasov simulation, the time step  $\Delta t_V$  is restricted by the CFL condition

$$\Delta t_V = \nu_{\text{CFL}} \min \left( \frac{\Delta_x}{u_{\text{max}}/a^2}, \min_j \left( \frac{\Delta_u}{|\phi_{x,j}|}, \frac{\Delta_u}{|\phi_{y,j}|}, \frac{\Delta_u}{|\phi_{z,j}|} \right) \right), \quad (11)$$

where  $\phi_{x,j}$ ,  $\phi_{y,j}$  and  $\phi_{z,j}$  represent numerical partial derivatives of gravitational potential  $\phi$  with respect to  $x$ ,  $y$ , and  $z$  at the  $j$ th mesh grid for the physical space, and  $\Delta_x = L_{\text{box}}/N_x^{1/3}$  and  $\Delta_u = 2u_{\text{max}}/N_u^{1/3}$  are the physical and velocity spacings of the Vlasov mesh grids, respectively. The CFL parameter  $\nu_{\text{CFL}}$  is set to  $\nu_{\text{CFL}} = 0.2$  as suggested in Tanaka et al. (2017).

Equations (4) and (8) are numerically integrated simultaneously with a time step given by

$$\Delta t = \min(\Delta t_N, \Delta t_V), \quad (12)$$

in a Kick–Drift–Kick (KDK) leapfrog manner (Quinn et al. 1997; Springel 2005). To integrate the system over a single time step  $t^n$  to  $t^{n+1} = t^n + \Delta t$ , we perform a number of steps sequentially in the following order:

1. We first compute the gravitational potential field  $\phi^n$  using the positions of the CDM particles and the distribution function of neutrinos at  $t = t^n$ .
2. Comoving velocities of CDM particles  $\dot{\mathbf{x}}^n$  are updated to  $\dot{\mathbf{x}}^{n+1/2}$  by one-half of the time step as

$$\dot{\mathbf{x}}^{n+1/2} = \dot{\mathbf{x}}^n \frac{1 - H^n \cdot \Delta t/2}{1 + H^n \cdot \Delta t/2} - \frac{\nabla\phi^n}{(a^n)^2} \frac{1}{1 + H^n \cdot \Delta t/2}, \quad (13)$$

where  $a^n$  and  $H^n$  are the scale factor and the Hubble parameter at  $t = t^n$ , respectively.

3. The distribution function of the neutrinos  $f^n(\mathbf{x}, \mathbf{u})$  at  $t = t^n$  is advected in the velocity space using the gravitational potential  $\phi^n$  at  $t = t^n$  by sequentially integrating Equations (7) over  $\Delta t/2$ , to yield an updated distribution function  $f^*(\mathbf{x}, \mathbf{u})$  formally given by

$$f^*(\mathbf{x}, \mathbf{u}) = f^n(\mathbf{x}, \mathbf{u} + \nabla\phi^n \cdot \Delta t/2). \quad (14)$$

4. The positions of the CDM particles  $\mathbf{x}^n$  are evolved to  $\mathbf{x}^{n+1}$  by a full time step of  $\Delta t$  using the comoving velocity  $\dot{\mathbf{x}}^{n+1/2}$  as

$$\mathbf{x}^{n+1} = \mathbf{x}^n + \dot{\mathbf{x}}^{n+1/2} \cdot \Delta t. \quad (15)$$

5. The neutrino distribution function is advected in the physical space by numerically integrating the advection Equation (6) by a time step of  $\Delta t$ . In this step, we set  $a^{n+1/2} = a(t^n + \Delta t/2)$  for the scale factor in Equation (6). The updated distribution function  $f^{**}(\mathbf{x}, \mathbf{u})$  is formally written as

$$f^{**}(\mathbf{x}, \mathbf{u}) = f^*(\mathbf{x} - \mathbf{u}/(a^{n+1/2})^2 \cdot \Delta t, \mathbf{u}). \quad (16)$$

6. Gravitational potential  $\phi^{n+1}$  at  $t = t^{n+1}$  is computed using the updated positions of the CDM particles and the neutrino distribution function  $f^{**}(\mathbf{x}, \mathbf{u})$  obtained in the previous steps. It should be noted that the density field of

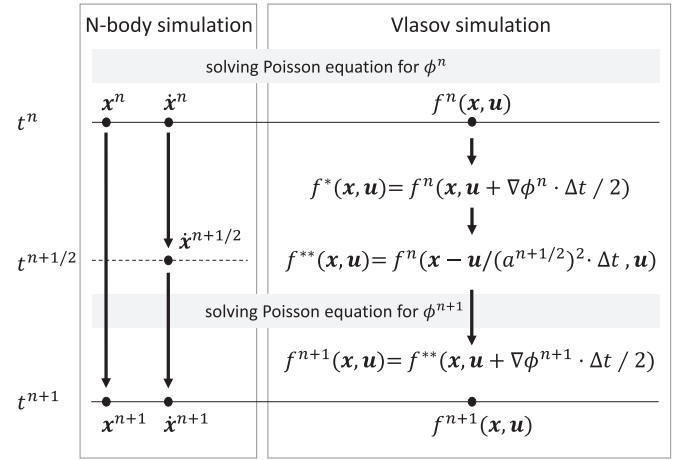


**Figure 1.** Schematic description of the time integration scheme of our hybrid  $N$ -body/Vlasov simulation.

neutrinos obtained from the distribution function  $f^{**}(\mathbf{x}, \mathbf{u})$  is identical to that from  $f^{n+1}(\mathbf{x}, \mathbf{u})$  computed in the next procedure.

7. Comoving velocities of CDM particles are evolved from  $\dot{\mathbf{x}}^{n+1/2}$  to  $\dot{\mathbf{x}}^{n+1}$  with  $\phi^{n+1}$  by a time step of  $\Delta t/2$  as

$$\dot{\mathbf{x}}^{n+1} = \dot{\mathbf{x}}^{n+1/2} \frac{1 - H^{n+1} \cdot \Delta t/2}{1 + H^{n+1} \cdot \Delta t/2} - \frac{\nabla\phi^{n+1}}{(a^{n+1})^2} \frac{1}{1 + H^{n+1} \cdot \Delta t/2}, \quad (17)$$

and the distribution function of neutrinos  $f^{**}(\mathbf{x}, \mathbf{u})$  is advected in the velocity space by sequentially integrating Equation (7) using the gravitational potential  $\phi^{n+1}$  at  $t = t^{n+1}$  to obtain the distribution function  $f^{n+1}(\mathbf{x}, \mathbf{u})$  at  $t = t^{n+1}$  written as

$$f^{n+1}(\mathbf{x}, \mathbf{u}) = f^{**}(\mathbf{x}, \mathbf{u} + \nabla\phi^{n+1} \cdot \Delta t/2). \quad (18)$$

Figure 1 shows a schematic description of numerical procedures in integrating  $N$ -body simulation and Vlasov simulation simultaneously by a single time step.

### 3. Cosmological Simulations

#### 3.1. Models

We assume a spatially flat cosmology with the present matter density parameter  $\Omega_m = 0.308$ , and that of baryons  $\Omega_b = 0.0484$ , the cosmological constant  $\Omega_\nu = 0.692$ , and the hubble constant  $h = 0.678$ . The model is consistent with the CMB observation by Planck satellite (Planck Collaboration et al. 2016).

We consider five cases with the total rest mass energy of three neutrino mass eigenstates of 0 eV (massless neutrinos), 0.1, 0.2, 0.3, and 0.4 eV. The present-epoch density parameters of neutrinos and CDM are given by

$$\Omega_\nu = 9.34 \times 10^{-3} \left( \frac{M_\nu c^2}{0.4 \text{ eV}} \right) \quad (19)$$

and  $\Omega_c = \Omega_m - \Omega_\nu$ , respectively. Table 1 summarize the set of numerical simulations. We run simulations with different volumes with the comoving side length  $L_{\text{box}}$  ranging from



**Table 1**  
Numerical Models Simulated in This Work

$L_{\text{box}}$	$M_\nu c^2$ (eV)	$\Omega_c$	$N_{\text{run}}$	$\sigma_8$
200 $h^{-1}$ Mpc	0.0	0.308	4	0.819
600 $h^{-1}$ Mpc			2	
1 $h^{-1}$ Gpc			1	
10 $h^{-1}$ Gpc			1	
200 $h^{-1}$ Mpc	0.1	0.306	4	0.804
600 $h^{-1}$ Mpc			2	
1 $h^{-1}$ Gpc			1	
10 $h^{-1}$ Gpc			1	
200 $h^{-1}$ Mpc	0.2	0.303	4	0.785
600 $h^{-1}$ Mpc			2	
1 $h^{-1}$ Gpc			1	
10 $h^{-1}$ Gpc			1	
200 $h^{-1}$ Mpc	0.3	0.301	4	0.765
600 $h^{-1}$ Mpc			2	
1 $h^{-1}$ Gpc			1	
10 $h^{-1}$ Gpc			1	
200 $h^{-1}$ Mpc	0.4	0.299	4	0.745
600 $h^{-1}$ Mpc			2	
1 $h^{-1}$ Gpc			1	
10 $h^{-1}$ Gpc			1	

**Note.**  $N_{\text{run}}$  is the number of realizations.

200  $h^{-1}$  Mpc to 10  $h^{-1}$  Gpc. We set the number of Vlasov mesh grids to  $(N_x, N_u) = (128^3, 64^3)$ , and the number of CDM particles to  $N_N = 1024^3$ . We perform convergence tests by comparing the simulations with different box sizes (Section 4.2). The mass of a single CDM particle is

$$m_{\text{CDM}} = 9.39 \times 10^8 f_{\text{CDM}} \left( \frac{L_{\text{box}}}{200 h^{-1} \text{ Mpc}} \right)^3 M_\odot, \quad (20)$$

where  $f_{\text{CDM}}$  is the CDM mass fraction given by  $f_{\text{CDM}} = \Omega_c / \Omega_m$ .

We assume that the masses of the three mass eigenstates are equal to each other. In practice, we follow the time evolution of only one distribution function because neutrinos in the three mass eigenstates can be treated identically under this assumption. We note that this is indeed a good approximation in the cases with  $M_\nu c^2 \gtrsim 0.2$  eV (Lesgourgues & Pastor 2006). However, if the total mass is smaller, i.e.,  $M_\nu c^2 \lesssim 0.1$  eV, the kinematic properties of the neutrinos cannot be represented accurately by a single distribution function. In the present study, we nevertheless assume an equal mass of neutrinos among the three eigenstates to avoid additional memory consumption necessary to handle multiple distribution functions in six-dimensional phase-space. The results of our simulations with  $M_\nu c^2 = 0.1$  eV should thus be regarded as being less accurate compared to the other cases in terms of the dynamical effect of massive neutrinos on the LSS formation.

### 3.2. Initial Conditions

We generate the initial conditions at the redshift of  $z_{\text{ini}} = 10$  for all our simulations listed in Table 1. We first compute the initial power spectra of density fluctuations of CDM and neutrinos separately using the CAMB software package (Lewis et al. 2000) for the cosmological parameters given in

Section 3.1. The spectral index of the primordial density fluctuations is set to be  $n_s = 0.96$ , and we normalize the fluctuation amplitudes such that the amplitude of the curvature perturbation power spectrum is  $\Delta_{\mathcal{R}} = 2.37 \times 10^{-9}$  at the pivot scale of  $k_p = 0.002 \text{ Mpc}^{-1}$ .

The initial positions of the CDM particles are determined by displacing the particles from a regular “lattice” distribution. The velocities are computed by using the Zel’dovich approximation. More accurate initial conditions can be generated by using a method based on second-order Lagrangian perturbation theory (2LPT, Crocce et al. 2006). Although our method without the second-order correction might yield slightly inaccurate power spectra of the initial density fluctuations at small length scales (Nishimichi et al. 2009), we expect that the overall impact to our simulations is limited, because strong nonlinear clustering of CDM is driven gravitationally at late epochs through to  $z = 0$ . We do not incorporate the effect of scale-dependent growth factor and growth rate in computing velocity fields of CDM and massive neutrinos (Zennaro et al. 2017), which is expected to be a minor impact on our initial conditions since the initial redshift is relatively low. In our future work, we will perform detailed comparison and convergence tests using multiple methods for the CDM initial condition. In the present paper, we focus on relative differences in various statistical quantities between the cases with relic neutrinos with different total masses (Section 4).

For neutrinos, we assume the initial distribution function at a time  $t_i$  is given by the Fermi–Dirac distribution as

$$f(\mathbf{x}, \mathbf{u}, t_i) = \frac{1 + \delta_\nu(\mathbf{x})}{N} F_{\text{FD}}((\mathbf{u} - \mathbf{u}_b)/a(t_i), t_i) \quad (21)$$

where  $\mathbf{u}_b(\mathbf{x})$  is the canonical bulk velocity of neutrinos at the location  $\mathbf{x}$ , and the normalization factor

$$N = \int F_{\text{FD}}((\mathbf{u} - \mathbf{u}_b(\mathbf{x}))/a(t_i), t_i) d^3\mathbf{u} \quad (22)$$

is introduced to satisfy the normalization of the neutrinos’ distribution function given by Equation (5). We do not consider the small distortion of the phase-space distribution induced during the relativistic and transrelativistic phases (Ma & Bertschinger 1994). The extent of velocity space  $u_{\text{max}}$  is set as  $u_{\text{max}} = 4 \sigma_u$  where  $\sigma_u$  is the dispersion of canonical velocity given by

$$\sigma_u^2 = \frac{\int u^2 f(\mathbf{x}, \mathbf{u}, t_i) d^3\mathbf{u}}{\int f(\mathbf{x}, \mathbf{u}, t_i) d^3\mathbf{u}}, \quad (23)$$

and is approximated as

$$\sigma_u \simeq 180 \left( \frac{m_\nu c^2}{1 \text{ eV}} \right)^{-1} \text{ km s}^{-1}. \quad (24)$$

Note that the peculiar velocity dispersion is given by

$$\sigma_v = 180(1 + z) \left( \frac{m_\nu c^2}{1 \text{ eV}} \right)^{-1} \text{ km s}^{-1}. \quad (25)$$

In practice, our simulations show that the estimated  $u_{\text{max}}$  is sufficiently large to enclose the velocity extent of the distribution function of neutrinos even after evolved to  $z = 0$ . As suggested by Yoshikawa et al. (2013), the velocity

resolution  $\Delta_u$  should satisfy the condition

$$\sigma_u / \Delta_u \gtrsim 5 \quad (26)$$

to reproduce the neutrino free streaming accurately. The choice of  $u_{\max} = 4\sigma_u$  yields the velocity resolution of  $\Delta_u = 2u_{\max}/N_u^{1/3} = \sigma_u/8$  satisfying the above condition.

### 3.3. Computational Facility

Our  $N$ -body/Vlasov hybrid simulations presented in this work are performed on the Oakforest-PACS (OfP) super-computer installed in Joint Center for Advanced High Performance Computing (JCAHPC).<sup>7</sup> Each computing node consists of a Intel Xeon Phi (Knights Landing) processor, 96 GiB DDR4 RAM, and 16 GiB of high-bandwidth MCDRAM. The simulations listed in Table 1 are run on 512 nodes, and typically consume 15 wall clock hours for the runs with  $L = 200h^{-1}$  Mpc.

## 4. Results

### 4.1. The Distribution of Neutrinos

Figure 2 shows the density distributions of CDM and neutrinos, as well as the distribution of massive DM halos with virial mass  $M > 10^{13} M_\odot$ , in the runs with  $L_{\text{box}} = 200h^{-1}$  Mpc. The plotted region is a slice with a width of  $\Delta_x$ , and the contours and color maps represent the overdensity of CDM and neutrinos, respectively. The region presented in Figure 2 contains the most massive DM halo with mass of  $1.26 \times 10^{15} M_\odot$  and  $9.84 \times 10^{14} M_\odot$  in the runs with  $M_\nu c^2 = 0.2$  eV and  $0.4$  eV, respectively, at  $z = 0$ . The distribution of neutrinos is much smoother than that of CDM owing to their large velocity dispersion. The neutrino density contrast is smaller for the smaller neutrino mass, but the maximum overdensity reaches  $\delta_\nu \sim 2$  at  $z = 0$ ; the large-scale nonlinear clustering is clearly seen even for the light neutrino model with  $M_\nu c^2 = 0.2$  eV.

Interestingly, the local neutrino density differs significantly in regions with similar CDM densities. We also find that massive DM halos tend to be located in neutrino-rich regions. In order to study this tendency further, we compute a joint probability distribution of the mass density fluctuation of neutrinos  $\delta_\nu$  and the number density fluctuations of DM halos defined as

$$\delta_h(\mathbf{x}) = \frac{n_h(\mathbf{x}) - \bar{n}_h}{\bar{n}_h}, \quad (27)$$

where  $n_h(\mathbf{x})$  is the number density of DM halos with virial mass greater than a certain threshold  $M_{h,\min}$ , and  $\bar{n}_h$  is the mean halo number density. Figure 3 shows the joint probability distribution of  $\delta_h$  and  $\delta_\nu$ , where  $M_{h,\min}$  is set to  $10^{12} M_\odot$  and both of  $\delta_h$  and  $\delta_\nu$  are smoothed over a comoving scale of  $R_s = 30h^{-1}$  Mpc with a top-hat filter. We also compute the mean relation of the neutrino density fluctuation  $\bar{\delta}_\nu(\delta_h)$  and its variance  $\overline{\delta_\nu^2}(\delta_h)$  as a function of  $\delta_h$  given by

$$\bar{\delta}_\nu(\delta_h) = \int P(\delta_h, \delta_\nu) \delta_\nu d\delta_\nu, \quad (28)$$

and

$$\overline{\delta_\nu^2}(\delta_h) = \int P(\delta_h, \delta_\nu) \delta_\nu^2 d\delta_\nu \quad (29)$$

where  $P(\delta_h, \delta_\nu)$  is the joint probability distribution function.  $\bar{\delta}_\nu(\delta_h)$  and  $\bar{\delta}_\nu(\delta_h) \pm [\overline{\delta_\nu^2}(\delta_h)]^{1/2}$  are plotted by solid and dotted lines, respectively, in each panel. We numerically derive several parameters that characterize the bias of neutrino mass density fluctuation relative to the number density fluctuation of DM halos following the nonlinear and stochastic model of Taruya & Suto (2000). The neutrino bias is defined as

$$b_{\text{cov}} = \frac{\langle \delta_\nu \delta_h \rangle}{\langle \delta_h^2 \rangle}, \quad (30)$$

and the nonlinearity and the stochasticity are given by, respectively,

$$\epsilon_{\text{nl}}^2 = \frac{\langle \delta_\nu^2 \rangle \langle \bar{\delta}_\nu^2 \rangle}{\langle \delta_\nu \delta_h \rangle^2} - 1, \quad (31)$$

and

$$\epsilon_{\text{scatt}}^2 = \frac{\langle \delta_h^2 \rangle \langle (\delta_\nu - \bar{\delta}_\nu)^2 \rangle}{\langle \delta_\nu \delta_h \rangle^2}. \quad (32)$$

We show the measured values of these quantities in each panel of Figure 3. We also compute the correlation coefficient between  $\delta_\nu$  and  $\delta_h$  defined as

$$r_{\text{corr}} = \frac{\langle \delta_\nu \delta_h \rangle}{\sqrt{\langle \delta_\nu^2 \rangle \langle \delta_h^2 \rangle}}. \quad (33)$$

Both  $\epsilon_{\text{nl}}^2$  and  $\epsilon_{\text{scatt}}^2$  are significantly smaller than unity, and hence the correlation coefficient, which scales as  $r_{\text{corr}} = (1 + \epsilon_{\text{nl}}^2 + \epsilon_{\text{scatt}}^2)^{-1/2}$ , is close to unity regardless of the neutrino mass, but the bias  $b_{\text{cov}}$  is smaller for less massive neutrinos. We note that these features are similar to the biasing relation between DM density field and DM halo number density studied by Taruya & Suto (2000) and Yoshikawa et al. (2001).

The mean  $\bar{\delta}_\nu - \delta_h$  relations are almost linear with small dispersions, suggesting that the local neutrino density can be inferred from the number density field of DM halos smoothed over a certain length scale for the cases with  $M_\nu c^2 \gtrsim 0.2$  eV, where we find  $\bar{\delta}_\nu(\delta_h) \gg [\overline{\delta_\nu^2}(\delta_h)]^{1/2}$  around  $\delta_h \simeq 1$ .

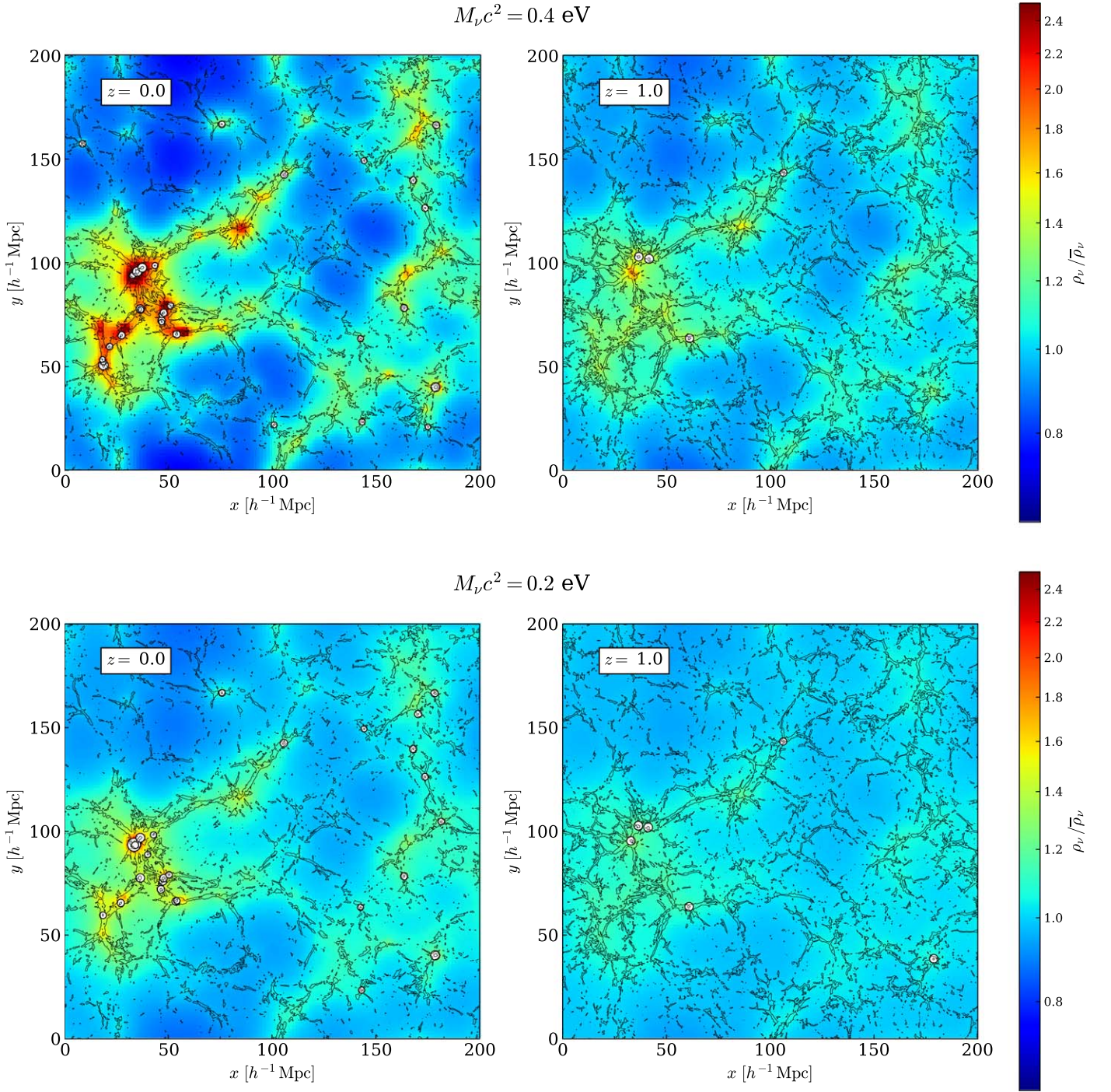
### 4.2. Velocity Dispersion of Neutrinos

Figure 4 shows the velocity dispersion  $\sigma_\nu$  of neutrinos (neutrino “temperature”) in the same slice of the simulation volume as Figure 2. Colors depict the velocity dispersion normalized by the cosmic mean (Equation (25)), the value of which is given in the top left of each panel. In the run with light neutrinos ( $M_\nu c^2 = 0.2$  eV),  $\sigma_\nu$  is lower in and around galaxy clusters, while we find higher  $\sigma_\nu$  in void regions. The trend is opposite in the run with “heavy” neutrinos ( $M_\nu c^2 = 0.4$  eV); we find higher  $\sigma_\nu$  in higher density regions.

These features can be explained by the fact that the mean velocity dispersion  $\bar{\sigma}_\nu$  ( $5.4 \times 10^3$  km s<sup>-1</sup> at  $z = 1$  and  $2.7 \times 10^3$  km s<sup>-1</sup> at  $z = 0$ ) is significantly larger than typical virial velocities of DM halos. Neutrinos in the high velocity tail of the distribution function streams out of DM halos, and then the velocity dispersion

<sup>7</sup> <http://jcahpc.jp/eng/index.html>





**Figure 2.** Density fields of CDM (contour) and neutrinos (color) in the runs with  $L_{\text{box}} = 200h^{-1} \text{ Mpc}$ ,  $M_\nu c^2 = 0.4 \text{ eV}$  (upper panels) and  $0.2 \text{ eV}$  (lower panels) at  $z = 0.0$  (left) and  $1.0$  (right). Color bars indicate the mass overdensity of neutrinos. Circles indicate positions of DM halos with a virial mass greater than  $10^{13} M_\odot$ . The radii of the circles are proportional to the virial radii of DM halos.

of neutrinos that are trapped within the halos effectively decreases. In the run with  $M_\nu c^2 = 0.4 \text{ eV}$ , the spatial variation of velocity dispersion at redshift  $z = 1$  is similar to that of  $M_\nu c^2 = 0.2 \text{ eV}$  runs at redshift  $z = 0$ . This is because the mean velocity dispersion is the same between the two cases at the respective epoch.

At  $z = 0$ , the run with  $M_\nu c^2 = 0.4 \text{ eV}$  looks significantly different from the results with  $M_\nu c^2 = 0.2 \text{ eV}$  at the same redshift. This is because the mean velocity dispersion already dropped to  $\sigma_v = 1.35 \times 10^3 \text{ km s}^{-1}$ , which is comparable to or smaller than the virial velocities of massive halos (rich galaxy

clusters). The neutrinos can gravitationally contract into the potential of the halos and of large-scale filamentary structures. This gravitational “heating” occurs in the high-density regions (Figure 4).

Figure 5 shows the relative-velocity field between CDM and neutrinos,  $|\mathbf{v}_c - \mathbf{v}_\nu|$ , where  $\mathbf{v}_c$  and  $\mathbf{v}_\nu$  is the bulk peculiar velocity of CDM and neutrinos, respectively. We calculate  $\mathbf{v}_c$  by averaging the peculiar velocities of  $N$ -body particles residing in the physical Vlasov mesh grids using the TSC assignment scheme. The neutrino streaming velocity  $\mathbf{v}_\nu$  is the mean averaged over entire

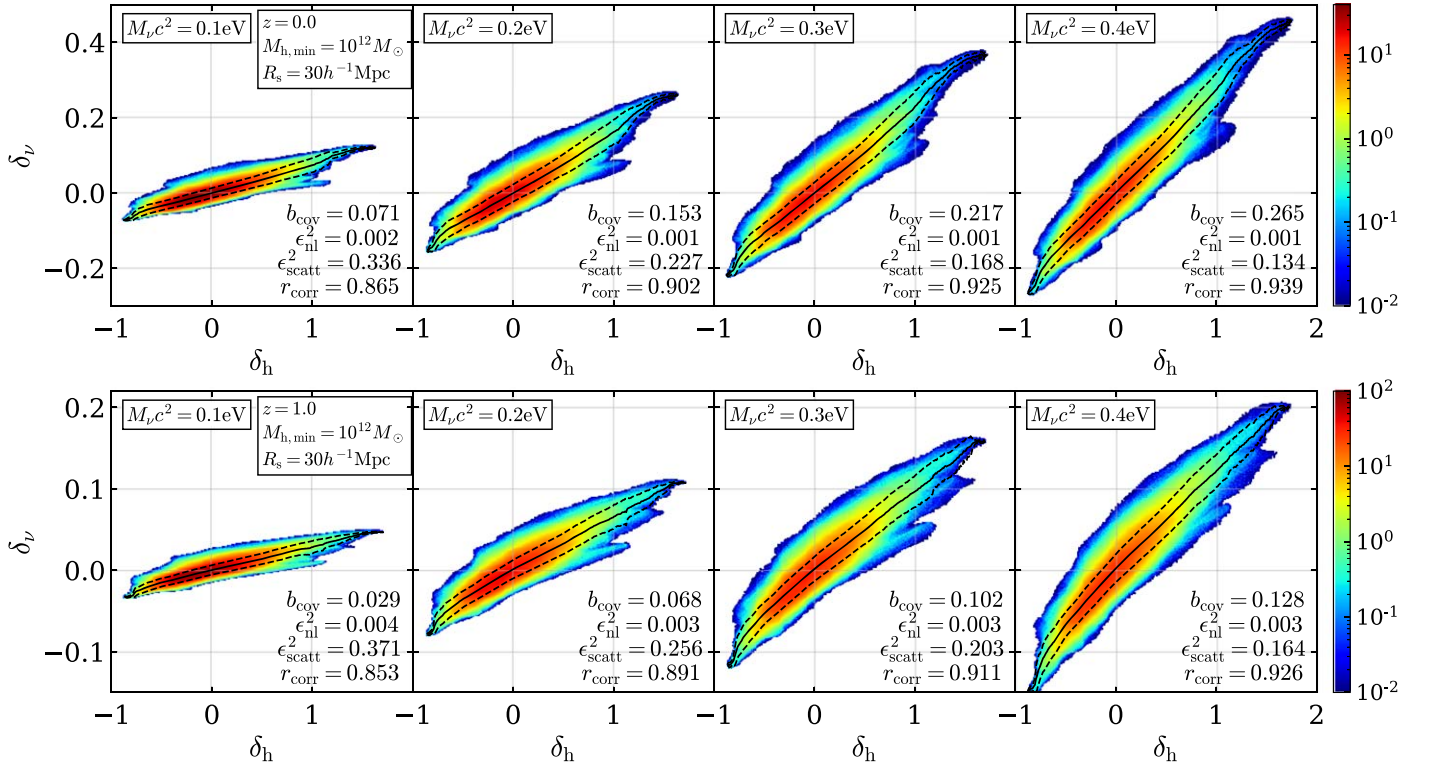


**Figure 3.** Probability distribution function of the number density of DM halos  $\delta_h$  and the mass density of neutrinos  $\delta_\nu$  at  $z = 0$  and  $z = 1$ . Both the quantities are smoothed with a smoothing scale of  $R_s = 30h^{-1} \text{ Mpc}$ . We consider DM halos with virial mass greater than  $10^{12} M_\odot$ . In each panel, the solid line indicates the mean value of neutrino density contrast for a given DM halo overdensity, and two dotted lines indicate the  $1\sigma$  dispersion of  $\delta_\nu$  around the mean.

velocity space. The relative streaming motions between CDM and neutrinos induce neutrino wakes in the downstream side of DM halos (Zhu et al. 2014). The relative motions are primarily driven by the gravitational clustering of CDM, and the induced “infall” motions of CDM determine the magnitude. This is manifested by the large relative velocities in the vicinity of filamentary structures and massive DM halos as can be seen in Figure 5.

On average, the relative-velocity magnitude is larger in runs with smaller neutrino mass, owing to the correspondingly larger neutrino velocity dispersion. Less massive neutrinos with large velocities are not trapped by the local gravitational potential generated by CDM.

We compute the power spectra of the relative velocity given by

$$\Delta_{v, cv}^2(k) = \frac{k^3}{2\pi^2} |\mathbf{v}_c(k) - \mathbf{v}_\nu(k)|^2, \quad (34)$$

where  $\mathbf{v}_c(k)$  and  $\mathbf{v}_\nu(k)$  are Fourier-transformed peculiar velocities of CDM and neutrinos, respectively. The computed power spectra are shown in Figure 6. The small amplitudes at  $k > 1h \text{ Mpc}^{-1}$  suggest that the relative velocity is coherent at 10–100 Mpc scales irrespective of neutrino masses. According to the linear perturbation theory, Fourier-transformed peculiar velocity of a component “s,”  $\mathbf{v}_s(k)$ , is given by

$$\mathbf{v}_s(k) = -\frac{ika}{k^2} \delta_s(k), \quad (35)$$

and thus the power spectrum of relative velocity is expressed as

$$\Delta_{v, cv}^2(k) = \frac{\mathcal{P}(k)k^3}{2\pi^2} \left[ \frac{\dot{T}_c(k) - \dot{T}_\nu(k)}{k} \right]^2, \quad (36)$$

where  $T_c(k)$  and  $T_\nu(k)$  are the transfer functions of CDM and neutrinos, and  $\mathcal{P}(k)$  is the primordial power spectrum of density perturbation. The linear theoretical prediction for power spectrum of relative velocity (Equation (36)) is also presented in Figure 6 in thick dotted lines, and is roughly consistent with our numerical results, although the linear theory predicts slightly higher power spectra than the numerical ones especially at smaller scales. Inman et al. (2015, 2017) also find that the simulated relative-velocity power spectra are in good agreement with linear perturbation theory at large scales with  $k \lesssim 0.1h \text{ Mpc}^{-1}$ , but the power amplitude is systematically smaller than the perturbation theory predictions at nonlinear scales. Nonlinear gravitational coupling between CDM and neutrinos may effectively suppress the velocity offset between the two components. We note that the power spectrum measurement is subject to the way of computing the velocity field of neutrinos from discrete particles (Zhang et al. 2015).

#### 4.3. Power Spectra of Density Fluctuations

Free-streaming of massive neutrinos causes characteristic suppression of the amplitude of matter density fluctuations. We compute the power spectra of the total matter (CDM + neutrinos) density at a wide range of wavenumbers using our simulation outputs. Figure 7 shows the power spectra of CDM density fluctuation at  $z = 0$  in the massless case obtained from the runs with  $L_{\text{box}} = 10h^{-1} \text{ Gpc}$ ,  $1h^{-1} \text{ Gpc}$  and  $200h^{-1} \text{ Mpc}$ . For box sizes of  $L_{\text{box}} = 200h^{-1} \text{ Mpc}$  and  $600h^{-1} \text{ Mpc}$ , we run four and two realizations and average the power spectra, respectively. For a given box size of  $L_{\text{box}}$ , the power spectrum



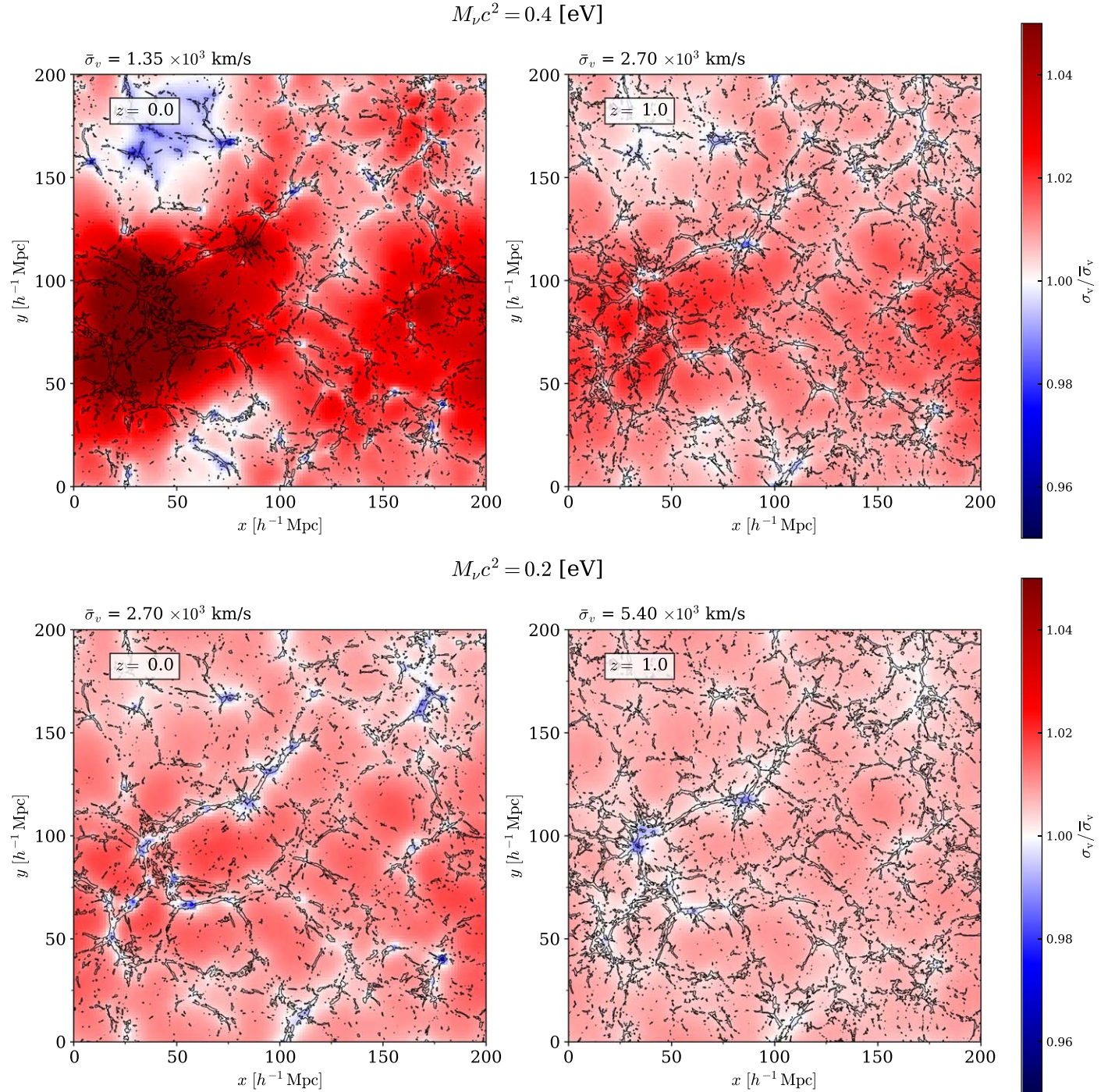


**Figure 4.** The neutrino velocity dispersion map in our runs with  $M_\nu c^2 = 0.4 \text{ eV}$  (upper panels) and  $0.2 \text{ eV}$  (lower panels) at  $z = 0$  and  $z = 1.0$ . Colors indicate the ratio of velocity dispersion with respect to the global mean indicated at the top left of each panel. Contours show the mass distribution of CDM.

is calculated in the wavenumber range of  $2\pi/L_{\text{box}} < k \leq k_{\text{ny}}$ , where  $k_{\text{ny}} \equiv \pi N_{\text{PM}}^{1/3}/L_{\text{box}}$  is the Nyquist wavenumber. Note that the long wavelength limit ( $k \simeq 2\pi/L_{\text{box}}$ ) of the computed power spectrum is affected by the sample variance due to the small number of modes, whereas the short wave limit ( $k \simeq k_{\text{ny}}$ ) is influenced by the finite spatial resolution of the simulations as well as force resolution of the PM  $N$ -body simulations. A direct way to check these numerical effects is to compare the power spectra with different box sizes. For example, the power spectra obtained from  $L_{\text{box}} = 10h^{-1} \text{ Gpc}$  and  $L_{\text{box}} = 1h^{-1} \text{ Gpc}$  runs agree with each other at

$2 \times 10^{-2} h \text{ Mpc}^{-1} < k < 6 \times 10^{-2} h \text{ Mpc}^{-1}$ , but we find that the amplitude at short wavelengths ( $k \gtrsim 10^{-1} h \text{ Mpc}^{-1}$ ) is significantly lower than the ones obtained in the other high-resolution runs. Considering these features of the power spectra of our simulations, we decided to construct a synthesized power spectrum by collecting the power spectra at the respective “reliable” wavenumber ranges from the results with  $L_{\text{box}} = 10h^{-1} \text{ Gpc}$ ,  $L_{\text{box}} = 1h^{-1} \text{ Gpc}$ , and  $L_{\text{box}} = 200h^{-1} \text{ Mpc}$  runs. The “reliable” ranges are indicated at the bottom of Figure 7.

In order to compute the total matter power spectra contributed both by CDM and neutrinos, we first compute



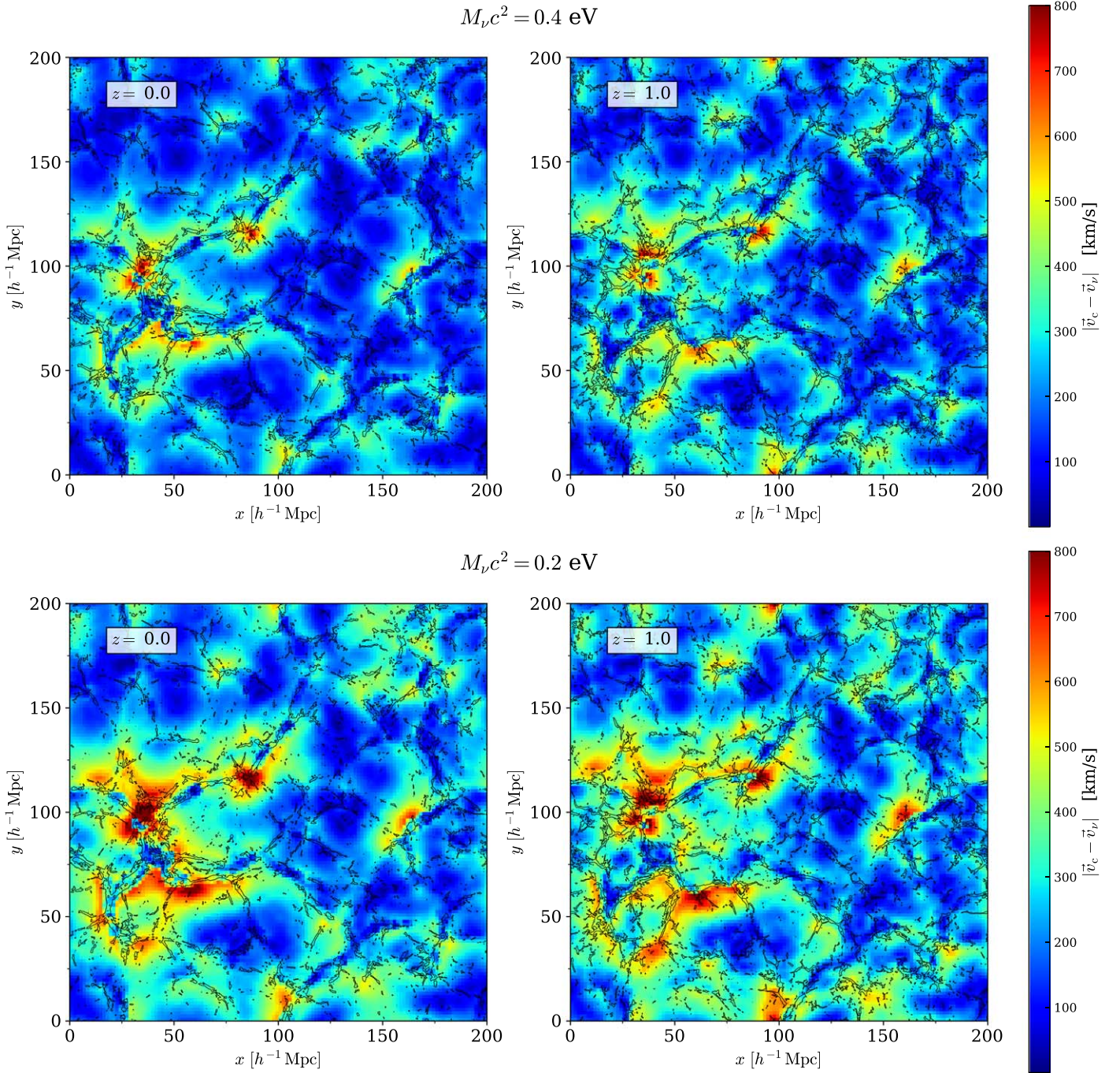
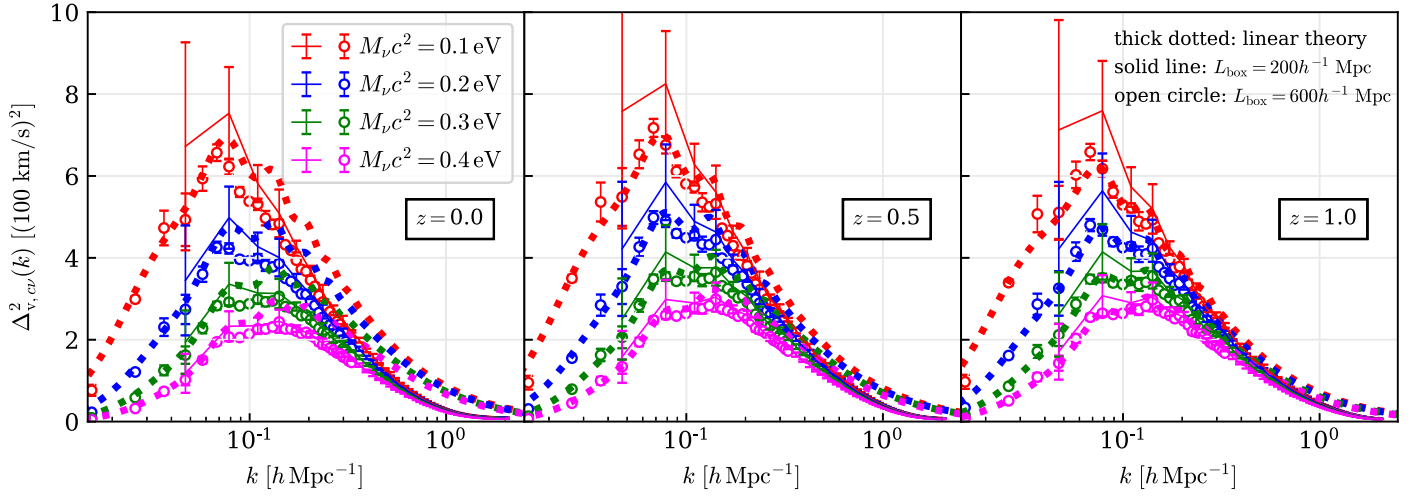


**Figure 5.** Relative velocities between CDM and neutrinos in the same regions presented in Figures 2 and 4.

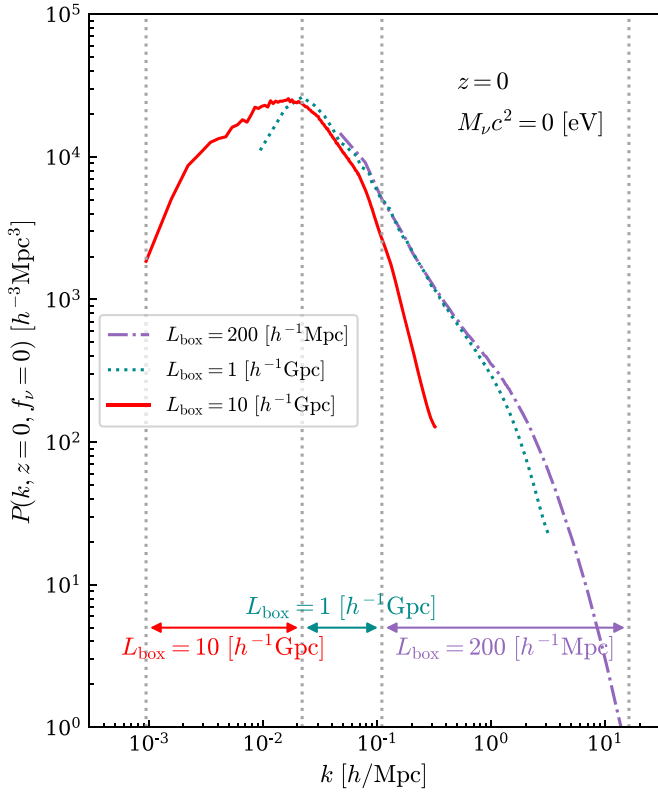
the CDM mass density by assigning the particle masses particles onto the regular  $N_{\text{PM}} = 1024^3$  mesh grids using the TSC mass assignment scheme. We then add the neutrino density to the mesh grids by up-sampling the neutrino density field with  $N_x$  mesh grids. The obtained total matter density field is Fourier-transformed to calculate the power spectrum, for which we correct the aliasing effect due to the finite number of mesh grids (Jing 2005).

Figure 8 shows the dimensionless power spectra of the neutrino density fluctuations  $k^3 P_\nu(k)$  calculated from the results of our  $N$ -body/Vlasov hybrid simulations, where  $P_\nu(k) = \langle |\delta_\nu(\mathbf{k})|^2 \rangle$ . Here, we synthesize the power spectra of the massive neutrinos

by combining the ones obtained by the simulations with  $L_{\text{box}} = 10 h^{-1} \text{ Gpc}$ ,  $1 h^{-1} \text{ Gpc}$  and  $200 h^{-1} \text{ Mpc}$  in the same manner described above. Notice the small discontinuous “jumps” at  $k \simeq 1.5 \times 10^{-1} h \text{ Mpc}^{-1}$  and  $2 \times 10^{-2} h \text{ Mpc}^{-1}$  that are caused by the synthesizing procedure. Since the density fluctuations of the neutrino component are intrinsically much smaller than that of the CDM component,  $P_\nu(k)$  can be significantly contaminated by shot noise, and can even be overwhelmed at small length scales in particle simulations (Viel et al. 2010; Yu et al. 2017; Banerjee et al. 2018). The neutrino density field in our  $N$ -body/Vlasov hybrid simulations is reproduced without the shot-noise contamination. Therefore, we



**Figure 6.** Power spectra of relative velocity between CDM and neutrinos obtained in the runs with  $L_{\text{box}} = 200 h^{-1} \text{ Mpc}$  (solid lines) and  $600 h^{-1} \text{ Mpc}$  (open circles). Error bars indicate the variance among the realizations. Thick dotted lines shows the predictions by the linear perturbation theory.



**Figure 7.** Power spectra of CDM density fluctuations obtained from runs with  $L_{\text{box}} = 10 h^{-1} \text{ Gpc}$  (solid),  $1 h^{-1} \text{ Gpc}$  (dotted), and  $200 h^{-1} \text{ Mpc}$  (dashed-dotted) for the massless neutrino cases. At the bottom, we indicate the ranges of wavenumbers adopted to generate the power spectrum from the simulations with different box sizes.

can obtain “clean” power spectra in a straightforward manner without any additional procedures such as subtraction of the shot-noise contribution (Yu et al. 2017). We find that our simulation results are consistent with linear perturbation theory at  $z > 2$ , but also find nonlinear clustering features at smaller scales of  $k \gtrsim 0.1 h \text{ Mpc}^{-1}$  at later epochs.

Figure 9 shows the ratios of the total matter power spectra with respect to those with massless neutrinos at redshifts of  $z = 0, 1$ , and  $2$  from left to right. We compare the power spectra with the results of the one-loop perturbation theory (Saito et al. 2008) for

$M_\nu c^2 = 0.1, 0.2$ , and  $0.4 \text{ eV}$ . The power spectra are consistent at large length scales of  $k < 0.1 h \text{ Mpc}^{-1}$ , but the perturbation theory predicts larger suppression at small scales. Our simulations show upturn features at  $k \gtrsim 1 h \text{ Mpc}^{-1}$ , as have been found also in  $N$ -body simulations (e.g., Brandbyge et al. 2008; Viel et al. 2010). As depicted in Figure 9 by dotted lines, the upturn features are in good agreement with the analytic model of Mead et al. (2016), which is based on the standard halo model (Peacock & Smith 2000; Seljak 2000; Cooray & Sheth 2002) with incorporating the effect of massive neutrinos and calibrated to match the power spectra obtained in COSMIC EMU simulations (Lawrence et al. 2010; Heitmann et al. 2014) and to simulations by Massara et al. (2014).

In order to examine quantitatively the effect of nonlinear CDM clustering, we perform additional  $N$ -body simulations with only the CDM component but with varying cosmological parameters  $(\sigma_8, \Omega_c) = (0.804, 0.306)$ ,  $(0.785, 0.303)$ ,  $(0.765, 0.301)$ , and  $(0.745, 0.299)$  where we also adjust  $\Delta_{\mathcal{R}}$  at the pivot scale for a targeted  $\sigma_8$ . These are the same combinations of  $\sigma_8$  and  $\Omega_c$  as adopted in the runs with massive neutrinos listed in Table 1. We compute the ratios of the CDM power spectra with respect to that with  $(\sigma_8, \Omega_c) = (0.819, 0.308)$  (the massless neutrino case) and show the results in Figure 10. It is remarkable that, at  $k \gtrsim 0.1 h \text{ Mpc}^{-1}$ , the power spectrum ratios of the CDM-only simulations closely resembles those of the CDM power spectra in  $N$ -body/Vlasov hybrid simulations. We conclude that the upturn feature observed in Figure 9 can be explained by the difference of nonlinear CDM clustering for different density parameter  $\Omega_c$  and the normalization of the density fluctuation  $\sigma_8$ . We note that our finding is consistent with the conclusion of Massara et al. (2014) based on their halo model.

#### 4.4. Mass Function of DM Halos

The DM halo mass function is a sensitive statistics to measure/constrain the neutrino mass. We identify DM halos in the runs with  $L_{\text{box}} = 200 h^{-1} \text{ Mpc}$  and  $600 h^{-1} \text{ Mpc}$  using the ROCKSTAR software package (Behroozi et al. 2013). We consider DM halos identified with at least 100 particles. The corresponding halo mass is  $9.39 \times 10^{10} f_{\text{CDM}} M_\odot$  and  $2.53 \times 10^{12} f_{\text{CDM}} M_\odot$  for the runs with  $L_{\text{box}} = 200 h^{-1} \text{ Mpc}$  and  $600 h^{-1} \text{ Mpc}$ , respectively.



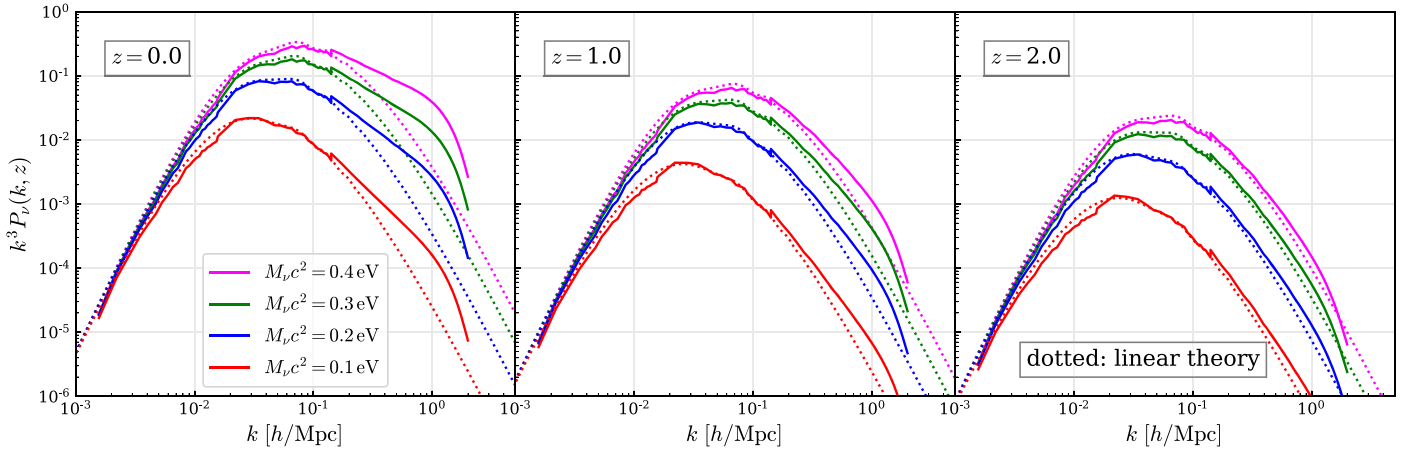


**Figure 8.** Synthesized power spectra of massive neutrinos obtained in our simulations at  $z = 0, 1$ , and  $2$  (solid lines). The dotted lines represent the linear perturbation theory predictions.

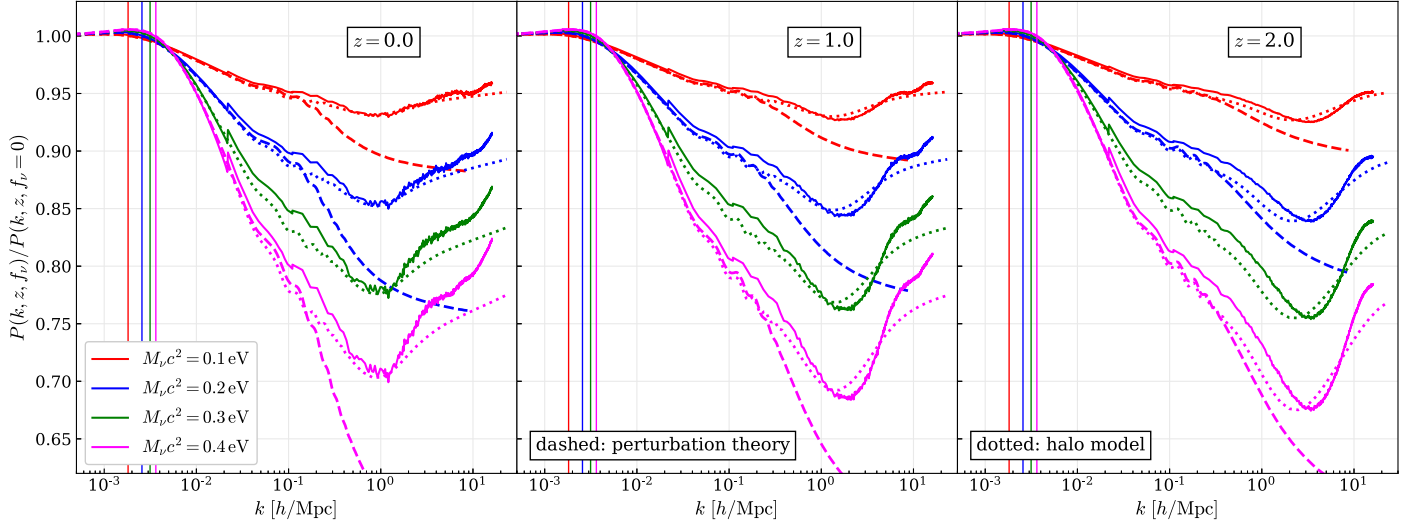


**Figure 9.** Ratios of total matter power spectrum with respect to the massless neutrino models at  $z = 0, 1$ , and  $2$ . The dashed lines represent the results from the one-loop perturbation theory of Saito et al. (2008), whereas the dotted lines are the halo model predictions of Mead et al. (2016). The vertical lines at the left of each panel indicate the wavenumbers corresponding to the maximum free-streaming scales, i.e., the distance traveled to the epoch of nonrelativistic transition.

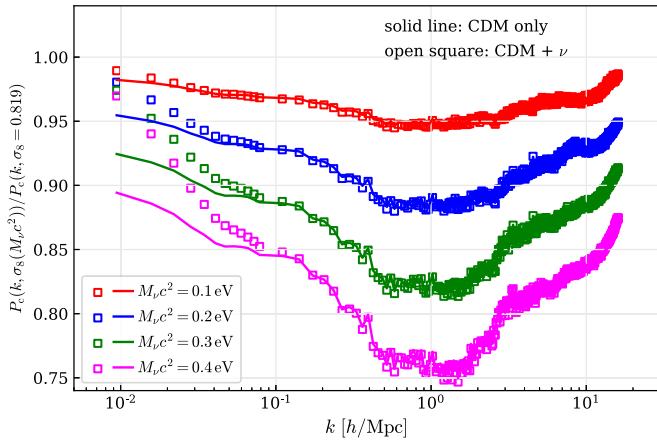


**Figure 10.** Ratios of power spectra of CDM density fluctuation in the CDM-only  $N$ -body simulations with  $\Omega_c$  and  $\sigma_8$  corresponding to the massive neutrino cases ( $M_\nu c^2 \neq 0$ ) with respect to the one with  $\sigma_8 = 0.819$  (the massless neutrino case) at  $z = 0$  (solid lines). The ratios of power spectra of CDM density fluctuation in the  $N$ -body/Vlasov hybrid simulation at  $z = 0$  with respect to the one with the massless neutrino case are also presented for comparison (open squares).

Figure 11 shows the mass function at  $z = 0, 0.5, 1.0$ , and  $2.0$ . We also present the ratio of the mass functions relative to the massless neutrino case in the lower panels. The mass functions of the massless cases are in good agreement with the analytic fit of Tinker et al. (2008).

There are less massive DM halos in models with massive neutrinos. We compare our simulation result for  $M_\nu c^2 = 0.1$  eV with the model of Ichiki & Takada (2012). Their model assumes spherical top-hat collapse in the presence of massive neutrinos.<sup>8</sup> The overall good agreement at  $z = 0$  suggests that the suppression at large mass scales is caused by the effective “drag” by free-streaming neutrinos. The mass function for the  $M_\nu c^2 = 0.3$  eV model is also consistent with the  $N$ -body simulation results of Costanzi et al. (2013), although the comparison can be made only at  $M > 2 \times 10^{13} M_\odot$ . It should be noted that the mass functions around  $M \simeq 10^{11} M_\odot$  might be affected by the mild force resolution of the PM scheme adopted in our  $N$ -body simulations.

<sup>8</sup> Ichiki & Takada (2012) assume the inverted mass hierarchy in which only two neutrino species have mass and the other one is massless. This is different from our setting in which three species have equal masses.

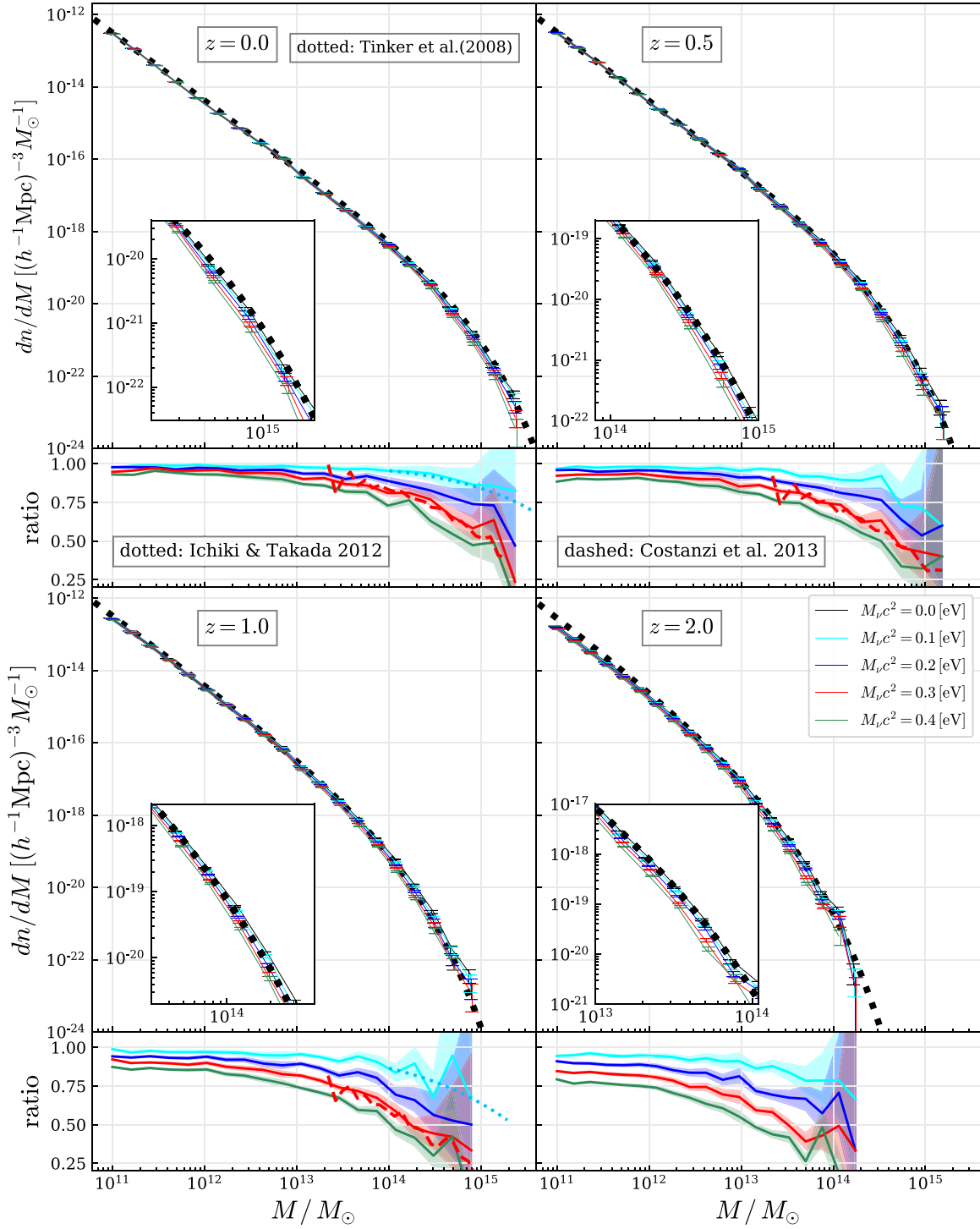


**Figure 11.** Mass functions of DM halos at redshifts of  $z = 0.0, 0.5, 1.0$ , and  $2.0$  (from left to right) are shown in upper panels, where dotted lines indicate mass functions modeled by Tinker et al. (2008). Error bars indicate the  $1\sigma$  statistical uncertainty. Lower panels depict ratios of mass functions relative to massless neutrino cases, where the shaded regions represent the  $1\sigma$  uncertainty around the mean values shown in the solid lines. In lower panel, we also plot theoretical predictions given by Ichiki & Takada (2012) with  $M_\nu c^2 = 0.1$  eV at redshift  $z = 0$  and  $1$  (dotted lines), and numerical results obtained by conventional  $N$ -body simulations (Costanzi et al. 2013) with  $M_\nu c^2 = 0.3$  eV at  $z = 0.0, 0.5$ , and  $1.0$  (dashed lines) for comparison.

The fact that the ratios of power spectra of density fluctuation with respect to the massless neutrino case can be explained by the nonlinear clustering of the CDM component as shown in Figure 10 motivates us to verify whether the same argument can be also applied to the ratios of DM halo mass functions presented in Figure 11. Figure 12 shows ratios of DM halo mass functions with sets of  $\sigma_8$  and  $\Omega_c$  for massive neutrino

cases in Table 1 with respect to the massless neutrino case with  $(\sigma_8, \Omega_c) = (0.819, 0.308)$  in dashed lines, where the DM halo mass functions are computed using the analytical fit by Tinker et al. (2008) at redshift of  $z = 0$ . The ratios are consistent with the ones obtained with our  $N$ -body/Vlasov hybrid simulations depicted by the filled squares, implying that the decrements of massive DM halos in massive neutrino cases relative to the

**Table 2**  
Comparison of Computational Resources and Spatial Resolution of Neutrino Distribution with Conventional  $N$ -body Simulations

Numerical Scheme	Computational Time	Memory Size	Spatial Resolution of Neutrino
$N$ -body w/o neutrinos	1	1	...
$N$ -body+Vlasov ( $N_x = N_c/8^3$ , $N_u = 64^3$ )	$\simeq 1 + 5 \left( \frac{8^3 N_c}{N_c} \right) \left( \frac{N_u}{64^3} \right) \left( \frac{\log 1024^3}{\log N_c} \right)$	$1 + 32 \left( \frac{8^3 N_c}{N_c} \right) \left( \frac{N_u}{64^3} \right)$	$\frac{L_{\text{box}}}{N_c^{1/3}} = 8 \left( \frac{N_c^{1/3}}{8 N_c^{1/3}} \right) \frac{L_{\text{box}}}{N_c^{1/3}}$
$N$ -body ( $N_\nu = N_c$ )	$\left( 1 + \frac{N_\nu}{N_c} \right) \frac{\log(N_c + N_\nu)}{\log N_c} \gtrsim 2$	$\gtrsim 1 + \frac{N_\nu}{N_c} = 2$	$4 \left( \frac{n_a}{64} \right)^{1/3} \left( \frac{N_c}{N_\nu} \right)^{1/3} \frac{L_{\text{box}}}{N_c^{1/3}}$
$N$ -body ( $N_\nu = 8N_c$ )	$\left( 1 + \frac{N_\nu}{N_c} \right) \frac{\log(N_c + N_\nu)}{\log N_c} \gtrsim 9$	$\gtrsim 1 + \frac{N_\nu}{N_c} = 9$	$2 \left( \frac{n_a}{64} \right)^{1/3} \left( \frac{8N_c}{N_\nu} \right)^{1/3} \frac{L_{\text{box}}}{N_c^{1/3}}$

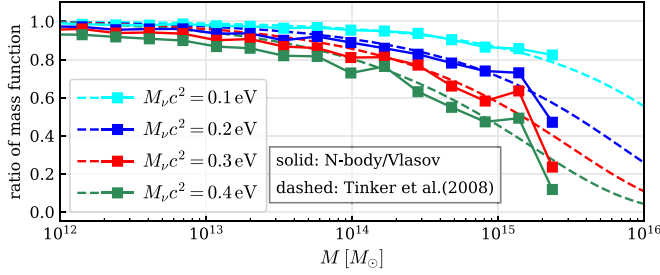


**Figure 12.** Ratios of DM halo mass functions obtained in our simulations relative to that in the massless neutrino case with  $(\Omega_c, \sigma_8) = (0.308, 0.819)$  (filled squares) are compared with those for DM mass functions with  $\Omega_c$  and  $\sigma_8$  corresponding to the massive neutrino cases calculated using the analytical fit by Tinker et al. (2008) (dashed lines).

massless neutrino case also can be explained by the difference in adopted  $\Omega_c$  and  $\sigma_8$ . This result is consistent with Castorina et al. (2014) in a sense that the universality of DM halo mass function holds even in the massive neutrino cases, as long as the rms density fluctuation of the CDM component, rather than that of the total one, is adopted to compute the DM halo mass function.

## 5. Computational Cost

In this section, we discuss advantages and disadvantages of our  $N$ -body/Vlasov hybrid simulations in comparison with conventional  $N$ -body simulations in terms of computational cost. The computational cost of these numerical simulations includes a variety of quantities such as CPU/wall clock time, required amount of memory, spatial resolution, parallelization efficiency, and so on. Since some of these depend on each other and also on technical properties of the hardwares on which simulations are performed, it is not very simple to compare different numerical schemes on different computational platforms. Therefore, we constrain ourselves to comparison with certain conditions. Namely, we study (1) the amount of memory needed to achieve a designated spatial resolution and (2) the computational time compared with respect to CDM-only simulations with the same number of CDM particles.

The computational cost of modern cosmological  $N$ -body simulations scales roughly as  $N \log N$ , where  $N$  is the number of particles.  $N$ -body simulations with massive neutrinos typically set  $N_\nu = N_c$  or  $N_\nu = 8N_c$  (e.g., Brandbyge et al. 2010; Bird et al. 2012; Inman et al. 2015), and the computational cost is roughly proportional to the total numbers of particles because the difference in the logarithmic factor is small. The memory requirement of  $N$ -body simulations is

estimated as follows. Sizes for the particle data and the PM mesh grids are both proportional to the number of particles, while that for the tree structure is proportional to  $\log N$  which has a small impact to the total memory requirement. Therefore, the overall memory requirement for a  $N$ -body simulations is roughly estimated to be proportional to the total number of particles (CDM+neutrinos).

The computational cost for solving the Vlasov equation with the directional splitting method (Equations (6) and (7)) is linearly proportional to the number of mesh grids in six dimension. Through our numerical experiments, we find that the CPU time required to integrate the Vlasov equation is about five times as large as that for the  $N$ -body simulation for the CDM component under our settings of the number of mesh grids ( $N_x = N_c/8^3 = 128^3$ , and  $N_u = 64^3$ ) and the number of CDM particles ( $N_c = 1024^3$ ). In terms of required amount of memory, each  $N$ -body particle has seven words (three for position, three for velocity, and one for particle index), and thus a  $N$ -body simulation needs a total of  $7N_c$  words and  $N_c$  words for the PM mesh grids. The Vlasov part uses  $N_x N_u$  words for the mesh grids. In our implementation, we adopt single precision floating-point numbers to store the distribution function in the Vlasov simulation, and adopt double-precision numbers for particle data in  $N$ -body simulations. Therefore, the total memory size of a  $N$ -body/Vlasov hybrid simulation is

$$8N_c + N_x N_u / 2 \quad (37)$$

in units of a double-precision word.

Table 2 compares the computational time and required memory size for our hybrid simulations and conventional  $N$ -body only simulations. We normalize the numbers by the corresponding ones for CDM-only simulations with the same number of particles. It should be noted that the values in the table refer to typical conditions, and they can vary by a factor of several depending on actual conditions such as the clustering amplitude of matter and velocity dispersion (or equivalently, mass) of neutrinos.

The computational time for our hybrid approach is in between those for  $N$ -body approach with  $N_\nu = N_c$  and  $N_\nu = 8N_c$ . The amount of required memory for the our hybrid approach is even larger than that of the  $N$ -body approach with  $N_\nu = 8N_c$ , but by only a factor of a few.

Another important issue we have to consider is the spatial resolution of neutrino distribution and the level of numerical shot noise. In our  $N$ -body/Vlasov hybrid simulations, the spatial resolution is set by the spatial mesh spacing of Vlasov mesh grids,  $L_{\text{box}}/N_x^{1/3}$ , and the numerical solutions are practically noiseless. On the other hand, in conventional  $N$ -body simulations, physical quantities such as density and



velocity fields of neutrinos are obtained by averaging over a sufficiently large number particles within a certain averaging length scale. The number of particles used in the averaging procedure sets the shot-noise level of the derived physical quantities. Hence, there is a trade-off between the spatial resolution and the shot noise in the physical quantities. This is an intrinsic problem with particle-based simulations.

Unlike the strong clustering of CDM, the density fluctuation of neutrinos remains relatively small from the early universe through to the present epoch. When averaging over  $n_a$   $N$ -body particles, the smoothing scale is approximately estimated to be  $n_a^{1/3}$  times mean interparticle separation  $L_{\text{box}}/N_v^{1/3}$ , and the fractional uncertainty of the averaged quantities is estimated to be  $n_a^{-1/2}$  assuming the Poissonian statistics. Therefore, if we adopt  $n_a = 64$ , the spatial resolution of the neutrino component is 4 times the mean interparticle separation. The fractional shot-noise level is then  $\simeq 12.5\%$ . In Table 2, we compare the effective spatial resolution of our  $N$ -body/Vlasov hybrid simulations and of conventional  $N$ -body simulations. With the current setting of  $N_c$  and  $N_x$ , the spatial resolution of our hybrid simulations is eight times the mean separation of the CDM particles. The spatial resolution in conventional  $N$ -body simulations is four and two times the mean separation of CDM particles for  $N_v = N_c$  and  $N_v = 8N_c$ , respectively, which is better than that in our hybrid approach, but the level of shot noise leaves  $\simeq 10\%$  uncertainty.

## 6. Summary and Discussion

We have performed a set of cosmological simulations of the large-scale structure formation with massive neutrinos. We solve the Vlasov–Poisson equations to follow the time evolution of the distribution function of neutrinos in the six-dimensional phase-space. Our simulations are able to reproduce accurately kinematic phenomena that strongly depend on the velocity distribution, such as free-streaming and collisionless damping of neutrinos and their wakes produced by the gravitational interaction with dark matter halos.

We use the simulations to study the effect of cosmological relic neutrinos on structure formation by varying the neutrino mass. We find that the neutrinos “condense” onto the large-scale structure (Yu et al. 2017). The neutrino mass density varies significantly across the cosmological volume, exhibiting nonlinear clustering. The neutrino-rich regions are strongly correlated with massive DM halos (galaxy clusters). We also find that the neutrino velocity dispersion  $\sigma_v$ , or the effective “temperature,” differs significantly depending on the neutrino mass. Interestingly,  $\sigma_v$  can be smaller than the cosmic mean in DM halos and filaments. This manifest selective escape of neutrinos in the high velocity tails of the distribution function, which leaves *cooler* neutrinos inside virialized objects.

We find larger relative streaming velocities in the case with lighter neutrinos because less massive neutrinos have a larger velocity dispersion whereas their bulk velocities are insensitive to local gravitational potential field. The resulting power spectra of the relative-velocity field is consistent with that predicted by linear perturbation theory at large length scales of  $k \lesssim 0.1 h/\text{Mpc}$ . The power amplitudes at smaller scales are significantly smaller than the linear theory prediction, suggesting nonlinear density–velocity coupling. These results are consistent with Inman et al. (2015, 2017).

The dynamical effect of massive neutrinos on the LSS formation is investigated in terms of damping of matter power spectra and the abundance of massive DM halos. The matter power spectra are found to be in good agreement with the first-order perturbation theory prediction of Saito et al. (2008) at wavenumbers of  $k < 0.1 h \text{ Mpc}^{-1}$ . Our simulation results exhibit departure from the prediction at smaller scales. We also find that such nonlinear features in matter power spectra are well reproduced by the halo model by Mead et al. (2016) and can be explained by the nonlinear clustering of the CDM component. Our  $N$ -body/Vlasov hybrid simulations enable us to compute the power spectra of the neutrino component without numerical shot noise. We find that the power spectra are consistent with the prediction of linear perturbation theory at high redshift ( $z > 2$ ), but show significant nonlinear evolution at  $k \gtrsim 0.1 h \text{ Mpc}$  at lower redshift.

As for the halo abundance, it is found that the mass function of DM halos is decreased under the presence of massive neutrinos and that the decrement is larger for more massive DM halos and for larger neutrino masses and is found to be consistent with previous numerical simulation by Costanzi et al. (2013) and also with the analytical prediction based on the spherical top-hat collapse model in the mixture of CDM and massive neutrinos (Ichiki & Takada 2012).

Overall, the results obtained by our  $N$ -body/Vlasov hybrid simulations agree well with those of  $N$ -body only simulations. It is encouraging that the two, completely different approaches to reproduce the dynamics of massive neutrinos in the LSS formation yield essentially consistent results. Conventional  $N$ -body simulations are not severely compromised by the shot noise due to coarse particle sampling as long as the statistical quantities of the dark matter density field and of dark halos are concerned. Our  $N$ -body/Vlasov hybrid approach has an advantage in reproducing kinematic phenomena in which the phase-space structure of neutrinos directly affect the dynamics. Generation of neutrino wakes is one such example. We continue exploring the nonlinear dynamics of collisionless systems such as neutrinos and hot/warm dark matter (WDM).

We thank the anonymous referee for his/her valuable comments on the earlier drafts of the manuscript. We also thank Shunsuke Hozumi for fruitful discussion in the early stage of this project. This research is supported by the Grant-in-Aid for Scientific Research by the JSPS KAKENHI grant No. JP18H04336 and by MEXT as “Priority Issue on Post-K computer” (Elucidation of the Fundamental Laws and Evolution of the Universe) and as “Program for Promoting Researches on the Supercomputer Fugaku” (Toward a unified view of the universe: from large-scale structures to planets). ST acknowledges support from JST AIP Acceleration Research grant No. JP 20317829. Numerical simulations presented in this paper are performed on computational resources of the K computer provided by the RIKEN Center for Computational Sciences through the HPCI System Research project (project ID:hp170231, hp180049, and hp190161). This research also uses computational resources of the Oakforest-PACS through the HPCI System Research Project (project ID:hp170123 and hp190093) and Multidisciplinary Cooperative Research Program in Center for Computational Sciences, University of Tsukuba.

## Appendix

### Choice of Velocity Coordinate in Cosmological Vlasov Equation

In the main text, we adopt the cosmological Vlasov equation in the form of Equation (4) where the canonical velocity  $\mathbf{u} = a^2\dot{\mathbf{x}}$  is used. One can also choose the peculiar velocity  $\mathbf{v} = a\dot{\mathbf{x}}$  as a velocity coordinate of the Vlasov equation, which can then be rewritten as

$$\frac{\partial \hat{f}}{\partial t} + \frac{\mathbf{v}}{a} \cdot \frac{\partial \hat{f}}{\partial \mathbf{x}} - \left[ H\mathbf{v} + \frac{\nabla \phi}{a^2} \right] \cdot \frac{\partial \hat{f}}{\partial \mathbf{v}} = 0, \quad (\text{A1})$$

where  $\hat{f}(\mathbf{x}, \mathbf{v}, t)$  is the distribution function as a function of  $\mathbf{x}$ ,  $\mathbf{v}$  and  $t$ . It is related to  $f(\mathbf{x}, \mathbf{u}, t)$  in Equation (4) as  $\hat{f}(\mathbf{x}, \mathbf{v}, t) = af(\mathbf{x}, \mathbf{u}, t)$ .

Although Equations (4) and (A1) are physically equivalent with each other, the choice of velocity coordinate is of critical importance in numerical simulations. Since we adopt a finite-volume method to solve the Vlasov equation, we need to determine the extent of velocity space *before* running a simulation so that the predefined velocity space covers the actual velocity distribution realized in the numerical simulation. In the light of this, Equation (4) is suitable for simulations with massive neutrinos, because their velocity dispersion is much larger than their typical bulk velocities, and because the dispersion of canonical velocity  $\mathbf{u} = a^2\dot{\mathbf{x}}$  remains roughly constant during the initial, linear evolution phase.

CDM or WDM; their bulk velocity is much larger than their thermal velocity dispersion contrary to the case with massive neutrinos, matter distribution in the canonical velocity space quickly changes due to the quadratic dependence on the scale factor  $a(t)$ , and eventually exceeds the pre-determined extent of the numerical “velocity” space. We find that Vlasov simulations of CDM and WDM are successfully performed by numerically integrating Equation (A1), and should be presented in our future works.

### ORCID iDs

Kohji Yoshikawa  <https://orcid.org/0000-0003-0389-5551>  
 Satoshi Tanaka  <https://orcid.org/0000-0003-2442-8784>  
 Naoki Yoshida  <https://orcid.org/0000-0001-7925-238X>  
 Shun Saito  <https://orcid.org/0000-0002-6186-5476>

### References

Alam, S., Ata, M., Bailey, S., et al. 2017, *MNRAS*, **470**, 2617  
 Ali-Haïmoud, Y., & Bird, S. 2013, *MNRAS*, **428**, 3375  
 Aviles, A., & Banerjee, A. 2020, arXiv:2007.06508  
 Banerjee, A., & Dalal, N. 2016, *JCAP*, **11**, 015  
 Banerjee, A., Powell, D., Abel, T., & Villaescusa-Navarro, F. 2018, *JCAP*, **9**, 028  
 Behroozi, P. S., Wechsler, R. H., & Wu, H.-Y. 2013, *ApJ*, **762**, 109  
 Beutler, F., Saito, S., Brownstein, J. R., et al. 2014, *MNRAS*, **444**, 3501  
 Bird, S., Viel, M., & Haehnelt, M. G. 2012, *MNRAS*, **420**, 2551  
 Blas, D., Garny, M., Konstandin, T., & Lesgourgues, J. 2014, *JCAP*, **2014**, 039  
 Boyle, A., & Komatsu, E. 2018, *JCAP*, **2018**, 035  
 Brandbyge, J., & Hannestad, S. 2009, *JCAP*, **5**, 002  
 Brandbyge, J., & Hannestad, S. 2010, *JCAP*, **1**, 021  
 Brandbyge, J., Hannestad, S., Haugbølle, T., & Thomsen, B. 2008, *JCAP*, **2008**, 020  
 Brandbyge, J., Hannestad, S., Haugbølle, T., & Wong, Y. Y. 2010, *JCAP*, **2010**, 014

Castorina, E., Sefusatti, E., Sheth, R. K., Villaescusa-Navarro, F., & Viel, M. 2014, *JCAP*, **2014**, 049  
 Chudaykin, A., & Ivanov, M. M. 2019, *JCAP*, **2019**, 034  
 Colombi, S., & Alard, C. 2017, *JPhPh*, **83**, 705830302  
 Colombi, S., & Touma, J. 2014, *MNRAS*, **441**, 2414  
 Cooray, A., & Sheth, R. 2002, *PhR*, **372**, 1  
 Costanzi, M., Villaescusa-Navarro, F., Viel, M., et al. 2013, *JCAP*, **2013**, 012  
 Crocce, M., Pueblas, S., & Scoccimarro, R. 2006, *MNRAS*, **373**, 369  
 Dupuy, H., & Bernardeau, F. 2015, *JCAP*, **2015**, 053  
 Filbet, F., & Sonnendrücker, E. 2003, *CoPhC*, **150**, 247  
 Font-Ribera, A., McDonald, P., Mostek, N., et al. 2014, *JCAP*, **2014**, 023  
 Führer, F., & Wong, Y. Y. 2015, *JCAP*, **2015**, 046  
 Fujiwara, T. 1981, *PASJ*, **33**, 531  
 Fujiwara, T. 1983a, *PASJ*, **35**, 547  
 Fujiwara, T. 1983b, *PhPh*, **70**, 603  
 Fukuda, Y., Hayakawa, T., Ichihara, E., et al. 1998, *PhRvL*, **81**, 1562  
 Heitmann, K., Lawrence, E., Kwan, J., Habib, S., & Higdon, D. 2014, *ApJ*, **780**, 111  
 Hockney, R. W., & Eastwood, J. W. 1981, *Computer Simulation Using Particles* (New York: McGraw-Hill)  
 Hu, W., Eisenstein, D. J., & Tegmark, M. 1998, *PhRvL*, **80**, 5255  
 Ichiki, K., & Takada, M. 2012, *PhRvD*, **85**, 063521  
 Ichiki, K., Takada, M., & Takahashi, T. 2009, *PhRvD*, **79**, 023520  
 Inman, D., Emberson, J. D., Pen, U.-L., et al. 2015, *PhRvD*, **92**, 023502  
 Inman, D., Yu, H.-R., Zhu, H.-M., et al. 2017, *PhRvD*, **95**, 083518  
 Ivanov, M. M., Simonović, M., & Zaldarriaga, M. 2020, *PhRvD*, **101**, 083504  
 Jing, Y. P. 2005, *ApJ*, **620**, 559  
 Lawrence, E., Heitmann, K., White, M., et al. 2010, *ApJ*, **713**, 1322  
 Lesgourgues, J., Matarrese, S., Pietroni, M., & Riotto, A. 2009, *JCAP*, **2009**, 017  
 Lesgourgues, J., & Pastor, S. 2006, *PhR*, **429**, 307  
 Levi, M., & Vlah, Z. 2016, arXiv:1605.09417  
 Lewis, A., Challinor, A., & Lasenby, A. 2000, *ApJ*, **538**, 473  
 Ma, C.-P., & Bertschinger, E. 1994, *ApJ*, **429**, 22  
 Massara, E., Villaescusa-Navarro, F., & Viel, M. 2014, *JCAP*, **2014**, 053  
 McCarthy, I. G., Bird, S., Schaye, J., et al. 2018, *MNRAS*, **476**, 2999  
 Mead, A. J., Heymans, C., Lombriser, L., et al. 2016, *MNRAS*, **459**, 1468  
 Namikawa, T., Saito, S., & Taruya, A. 2010, *JCAP*, **2010**, 027  
 Nishimichi, T., Shirata, A., Taruya, A., et al. 2009, *PASJ*, **61**, 321  
 Palanque-Delabrouille, N., Yèche, C., Schöneberg, N., et al. 2020, *JCAP*, **2020**, 038  
 Peacock, J. A., & Smith, R. E. 2000, *MNRAS*, **318**, 1144  
 Peloso, M., Pietroni, M., Viel, M., & Villaescusa-Navarro, F. 2015, *JCAP*, **2015**, 001  
 Planck Collaboration, Ade, P. A. R., Aghanim, N., et al. 2016, *A&A*, **594**, A13  
 Planck Collaboration, Aghanim, N., Akrami, Y., et al. 2020, *A&A*, **641**, A6  
 Quinn, T., Katz, N., Stadel, J., & Lake, G. 1997, arXiv:astro-ph/9710043  
 Saito, S., Takada, M., & Taruya, A. 2008, *PhRvL*, **100**, 191301  
 Saito, S., Takada, M., & Taruya, A. 2009, *PhRvD*, **80**, 083528  
 Saito, S., Takada, M., & Taruya, A. 2011, *PhRvD*, **83**, 043529  
 Seljak, U. 2000, *MNRAS*, **318**, 203  
 Seljak, U., Slosar, A., & McDonald, P. 2006, *JCAP*, **2006**, 014  
 Senatore, L., & Zaldarriaga, M. 2017, arXiv:1707.04698  
 Shoji, M., & Komatsu, E. 2009, *ApJ*, **700**, 705  
 Springel, V. 2005, *MNRAS*, **364**, 1105  
 Takada, M., Komatsu, E., & Futamase, T. 2006, *PhRvD*, **73**, 083520  
 Tanaka, S., Yoshikawa, K., Minoshima, T., & Yoshida, N. 2017, *ApJ*, **849**, 76  
 Taruya, A., & Suto, Y. 2000, *ApJ*, **542**, 559  
 Thomas, S. A., Abdalla, F. B., & Lahav, O. 2010, *PhRvL*, **105**, 031301  
 Tinker, J., Kravtsov, A. V., Klypin, A., et al. 2008, *ApJ*, **688**, 709  
 Upadhye, A., Biswas, R., Pope, A., et al. 2014, *PhRvD*, **89**, 103515  
 Viel, M., Haehnelt, M. G., & Springel, V. 2010, *JCAP*, **6**, 015  
 Villaescusa-Navarro, F., Hahn, C., Massara, E., et al. 2020, *ApJS*, **250**, 2  
 Villaescusa-Navarro, F., Marulli, F., Viel, M., et al. 2014, *JCAP*, **2014**, 011  
 Wong, Y. Y. 2008, *JCAP*, **10**, 035  
 Wright, B. S., Winther, H. A., & Koyama, K. 2017, *JCAP*, **2017**, 054  
 Yoshikawa, K., Taruya, A., Jing, Y. P., & Suto, Y. 2001, *ApJ*, **558**, 520  
 Yoshikawa, K., Yoshida, N., & Umehara, M. 2013, *ApJ*, **762**, 116  
 Yu, H.-R., Emberson, J. D., Inman, D., et al. 2017, *NatAs*, **1**, 0143  
 Zennaro, M., Bel, J., Villaescusa-Navarro, F., et al. 2017, *MNRAS*, **466**, 3244  
 Zhang, P., Zheng, Y., & Jing, Y. 2015, *PhRvD*, **91**, 043522  
 Zhao, G.-B., Saito, S., Percival, W. J., et al. 2013, *MNRAS*, **436**, 2038  
 Zhu, H.-M., Pen, U.-L., Chen, X., Inman, D., & Yu, Y. 2014, *PhRvL*, **113**, 131301